Ab-initio structural optimization at finite temperatures based on anharmonic phonon theory: Application to the structural phase transitions of BaTiO$_3$

Ryota Masuki,[1, *] Takuya Nomoto,[2, †] Ryotaro Arita,[2, 3, ‡] and Terumasa Tadano[4, §]

[1]*Department of Applied Physics, The University of Tokyo,7-3-1 Hongo, Bunkyo-ku, Tokyo 113-8656, Japan*
[2]*Research Center for Advanced Science and Technology,*
The University of Tokyo, 4-6-1 Komaba Meguro-ku, Tokyo 153-8904, Japan
[3]*RIKEN Center for Emergent Matter Science, 2-1 Hirosawa, Wako, Saitama 351-0198, Japan*
[4]*CMSM, National Institute for Materials Science (NIMS), 1-2-1 Sengen, Tsukuba, Ibaraki 305-0047, Japan*
(Dated: December 20, 2022)

We formulate a first-principle scheme for structural optimization at finite temperature (T) based on the self-consistent phonon (SCP) theory, which accurately takes into account the effect of strong phonon anharmonicity. The T-dependence of the shape of the unit cell and internal atomic configuration is determined by minimizing the variational free energy in the SCP theory. At each optimization step, the interatomic force constants in the new structure are calculated without running additional electronic structure calculations, which makes the method dramatically efficient. We demonstrate that the thermal expansion of silicon and the three-step structural phase transitions in BaTiO$_3$ and its pressure-temperature (p-T) phase diagram are successfully reproduced. The present formalism will open the way to the non-empirical prediction of physical properties at finite T of materials having a complex structural phase diagram.

I. INTRODUCTION

Temperature dependence of crystal structure is one of the most fundamental problems in solid state physics. As the crystal structure changes, a wide variety of materials exhibit fascinating properties: Ferroelectric phase transitions in perovskite oxides [1–4], charge density wave in transition metal dichalcogenides [5–8], and Martensitic transformation in the shape-memory alloy [9–11] are a few representative examples. In addition to being an important topic for its fundamental interest and expected application, such as switches, memories, and piezoelectric devices [12–14], various exotic phenomena occur in the vicinity of structural phase transition. For example, the thermoelectric effect is enlarged by the transport anomaly due to the strong scattering of carriers [15–17]. Recent theoretical works claim that damped soft modes near structural phase transitions greatly enhance superconductivity [18, 19]. High-pressure high-T_c hydride superconductors [20–24] and the halide perovskite photovoltaics [25, 26] are also close to structural phase transitions. Nonempirical determination of T-dependent crystal structure is crucial for quantitatively understanding these phenomena and searching for related materials.

While the state-of-the-art structural optimization based on density functional theory (DFT) accurately calculates the crystal structure at zero temperature [27–33], it has been a significant challenge to predict crystal structures at finite temperatures because one needs to consider the strong anharmonicity in lattice vibrations. Anharmonicity refers to the third and higher-order terms of the Taylor expansion of the Born-Oppenheimer potential energy surface, which corresponds to

phonon-phonon interaction from a field-theoretical point of view. The finite-temperature phases of strongly anharmonic crystals often have unstable phonon modes, in which case the perturbative theory based on the harmonic approximation completely breaks down due to the imaginary frequency [34–37]. In addition, the nuclear quantum effect also has a significant impact on the structures of crystals and molecules that contains light atoms or those in the vicinity of the structural phase transition [38–41].

Ab initio molecular dynamics (AIMD) exactly treats the anharmonic effect, but it neglects the nuclear quantum effect. Additionally, AIMD calculations often suffer from the finite-size effect of the supercell and the stochastic errors of the sampling, which makes it infeasible to obtain accurate results with reasonable computational costs. Recently, machine-learning potentials which can efficiently calculate atomic forces and energies with first-principles quality have been developed to overcome these difficulties [42–45]. Nonetheless, the computational cost to generate the potentials is still high because it requires a large set of training data, and assessing the quality of the generated potentials requires special expertise.

The self-consistent phonon (SCP) theory takes into account the nuclear quantum effect and the anharmonic effect in a self-consistent way [46–49], which have been shown to accurately reproduce the vibrational properties of strongly anharmonic materials even with imaginary harmonic frequencies [35–37, 50, 51]. While several different methods and implementations have been presented [35–37, 52–57], we employ the momentum-space SCP theory [37, 56], which is suitable for calculation on a fine temperature grid due to the efficiency of SCP calculations at each temperature. Additionally, the momentum-space formulation takes advantage of the Brillouin zone interpolation of being able to efficiently obtain results that are free from the finite size effect of the DFT supercells.

In this paper, we formulate a theory of structural optimization at finite temperature based on the SCP theory in momentum space. The internal coordinates and the shape of the unit cell are optimized to minimize the SCP free energy with

* masuki-ryota774@g.ecc.u-tokyo.ac.jp
† nomoto@ap.t.u-tokyo.ac.jp
‡ arita@riken.jp
§ TADANO.Terumasa@nims.go.jp

the aid of its gradient with respect to the structural degrees of freedom. At each optimization step, the interatomic force constants (IFCs) in the updated structure are calculated from the IFCs in the reference structure without running additional DFT calculations, which makes our method highly efficient. We call the process of updating the IFCs as IFC renormalization. The momentum-space SCP theory combined with the IFC renormalization technique remarkably extends the applicability of our method to complex materials with many degrees of freedom.

We then apply the present method to the thermal expansion of silicon and the three-step structural phase transition of BaTiO$_3$, which shows good agreement with experimental results. BaTiO$_3$ is a perovskite oxide which is known as one of the most representative ferroelectrics [13, 58, 59]. Under ambient pressure, BaTiO$_3$ displays the cubic phase at high temperatures. When cooled, it exhibits transitions to the tetragonal phase at around 390 K, then to the orthorhombic phase at around 270 K, and finally to the rhombohedral phase at around 180 K [13]. We show that the developed method successfully reproduces the three structural phase transitions and the temperature dependence of the lattice constants as well as the spontaneous polarization of BaTiO$_3$. In addition, we perform calculations on BaTiO$_3$ under static pressure and demonstrate that our method well reproduces the experimental results of its p-T phase diagram.

II. THEORY

In this section, we explain the formulation of structural optimization at finite temperature based on momentum-space SCP theory. Starting from the Taylor expansion of the potential energy surface, we explain the process of updating interatomic force constants (IFCs) at each step in structural optimization, which we call the IFC renormalization. The process is essential to the efficiency of our method. In the end, the theory of structural optimization at finite temperature is presented based on the preparations.

A. Taylor expansion of the potential energy surface

In crystalline solids, in which the atoms are bound near their equilibrium positions, the Born-Oppenheimer potential energy surface can be Taylor-expanded in terms of the atomic displacement operator $\hat{u}_{R\alpha\mu}$. R denotes the position of the primitive cell to which the atom belongs. α is the atom index in the primitive cell and $\mu = x, y, z$. If we write the potential as $\hat{U}$, its Taylor expansion is

$$\hat{U} = \sum_{n=0}^{\infty} \hat{U}_n, \tag{1}$$

$\hat{U}_n$

$$= \frac{1}{n!} \sum_{\{R\alpha\mu\}} \Phi_{\mu_1\cdots\mu_n}(R_1\alpha_1, \cdots, R_n\alpha_n)\hat{u}_{R_1\alpha_1\mu_1} \cdots \hat{u}_{R_n\alpha_n\mu_n}$$

$$= \frac{1}{n!} \frac{1}{N^{n/2-1}} \sum_{\{k\lambda\}} \delta_{k_1+\cdots+k_n} \widetilde{\Phi}(k_1\lambda_1, \cdots, k_n\lambda_n)\hat{q}_{k_1\lambda_1} \cdots \hat{q}_{k_n\lambda_n}. \tag{2}$$

The expansion coefficients

$$\Phi_{\mu_1\cdots\mu_n}(R_1\alpha_1, \cdots, R_n\alpha_n) = \frac{\partial^n U}{\partial u_{R_1\alpha_1\mu_1} \cdots \partial u_{R_n\alpha_n\mu_n}}\bigg|_{u=0}, \tag{3}$$

are called the interatomic force constants (IFCs). The second-order, third-order and fourth-order terms are called the harmonic, cubic, and quartic terms, respectively. The normal coordinate operators

$$\hat{q}_{k\lambda} = \frac{1}{\sqrt{N}} \sum_{R\alpha\mu} e^{-ik\cdot R} \epsilon^*_{k\lambda,\alpha\mu} \sqrt{M_\alpha}\hat{u}_{R\alpha\mu}, \tag{4}$$

are introduced in the momentum space, where N is the number of primitive cells. Accordingly, the momentum-space representation of the interatomic force constants is defined as

$$\widetilde{\Phi}(k_1\lambda_1, \cdots, k_n\lambda_n)$$

$$= \frac{1}{N} \sum_{\{R\alpha\mu\}} \Phi_{\mu_1\cdots\mu_n}(R_1\alpha_1, \cdots, R_n\alpha_n)$$

$$\times \frac{\epsilon_{k_1\lambda_1,\alpha_1\mu_1}}{\sqrt{M_{\alpha_1}}} e^{ik_1\cdot R_1} \cdots \frac{\epsilon_{k_n\lambda_n,\alpha_n\mu_n}}{\sqrt{M_{\alpha_n}}} e^{ik_n\cdot R_n}$$

$$= \sum_{\{\alpha\mu\}} \frac{\epsilon_{k_1\lambda_1,\alpha_1\mu_1}}{\sqrt{M_{\alpha_1}}} \cdots \frac{\epsilon_{k_n\lambda_n,\alpha_n\mu_n}}{\sqrt{M_{\alpha_n}}}$$

$$\times \sum_{R_1\cdots R_{n-1}} \Phi_{\mu_1\cdots\mu_n}(R_1\alpha_1, \cdots, R_{n-1}\alpha_{n-1}, 0\alpha_n)e^{i(k_1\cdot R_1+\cdots+k_{n-1}\cdot R_{n-1})}.$$

where $\epsilon_{k\lambda,\alpha\mu}$ is the polarization vector of phonon mode $k\lambda$, which diagonalizes the harmonic dynamical matrix in the reference structure.

B. Changes in the crystal structure and the IFC renormalization

The SCP theory incorporates the vibrational free energy based on the Born-Oppenheimer approximation, which we use to consider the finite-temperature effect in crystal structures. Therefore, the IFCs, which determine the potential energy surface, play a crucial role in SCP calculations, as we later explain in more detail. In this section, we explain that it is possible to calculate the IFCs in updated crystal structures from the IFCs in the reference crystal structure [60].

We first consider the change of the internal coordinates of the atoms. We write the μ component of the atomic shift of the atom α as

$$q^{(0)}_{\alpha\mu} = \sqrt{M_\alpha}u^{(0)}_{\alpha\mu}. \tag{5}$$

Here, we assume that the atomic shift is commensurate to the primitive cell, i.e., $u_{\alpha\mu}^{(0)}$ is independent of the choice of primitive cell $\mathbf{R}$. When the crystal structure is updated in the structural optimization process, we re-define the atomic displacement operators $\hat{u}_{\mathbf{R}\alpha\mu}$ or $\hat{q}_{\mathbf{k}\lambda}$ as the displacements from the new crystal structure. This re-definition of displacement operators corresponds to substituting

$$\hat{q}_{\mathbf{k}\lambda} \leftarrow \begin{cases} \hat{q}_{\mathbf{k}\lambda} & (\mathbf{k} \neq 0) \\ \hat{q}_{\mathbf{k}\lambda} + \sqrt{N}q_\lambda^{(0)} & (\mathbf{k} = 0) \end{cases} \tag{6}$$

to Eq. (2), where

$$q_\lambda^{(0)} = \sum_{\alpha\mu} \epsilon_{0\lambda,\alpha\mu} q_{\alpha\mu}^{(0)}. \tag{7}$$

Thus, Eq. (2) in the reference structure is rewritten as

$$\hat{U}_n^{(q^{(0)}=0)} = \frac{1}{n!} \frac{1}{N^{n/2-1}} \sum_{\{\mathbf{k}\lambda\}} \delta_{\mathbf{k}_1+\cdots+\mathbf{k}_n} \widetilde{\Phi}^{(q^{(0)}=0)}(\mathbf{k}_1\lambda_1, \cdots, \mathbf{k}_n\lambda_n)$$
$$\times (\hat{q}_{\mathbf{k}_1\lambda_1} + \delta_{\mathbf{k}_1}\sqrt{N}q_{\lambda_1}^{(0)}) \cdots (\hat{q}_{\mathbf{k}_n\lambda_n} + \delta_{\mathbf{k}_n}\sqrt{N}q_{\lambda_n}^{(0)}). \tag{8}$$

Note that the normal-coordinate operators $\hat{q}_{\mathbf{k}\lambda}$ are defined in accordance with the atomic displacements in the updated structure. Properly rearranging the terms, we get

$$\hat{U} = \sum_{n=0}^{\infty} \hat{U}_n^{(q^{(0)})}, \tag{9}$$

$$\hat{U}_n^{(q^{(0)})} = \frac{1}{n!} \frac{1}{N^{n/2-1}} \sum_{\{\mathbf{k}\lambda\}} \delta_{\mathbf{k}_1+\cdots+\mathbf{k}_n}$$
$$\times \widetilde{\Phi}^{(q^{(0)})}(\mathbf{k}_1\lambda_1, \cdots, \mathbf{k}_n\lambda_n)\hat{q}_{\mathbf{k}_1\lambda_1} \cdots \hat{q}_{\mathbf{k}_n\lambda_n}, \tag{10}$$

$$\widetilde{\Phi}^{(q^{(0)})}(\mathbf{k}_1\lambda_1, \cdots, \mathbf{k}_n\lambda_n)$$
$$= \sum_m \frac{1}{m!} \sum_{\{\rho\}} \widetilde{\Phi}^{(q^{(0)}=0)}(\mathbf{k}_1\lambda_1, \cdots, \mathbf{k}_n\lambda_n, 0\rho_1, \cdots 0\rho_m)q_{\rho_1}^{(0)} \cdots q_{\rho_m}^{(0)} \tag{11}$$

Thus, the IFCs in the structure with atomic shifts, $\widetilde{\Phi}^{(q^{(0)})}$, can be obtained using the IFCs in the reference structure without atomic shifts ($\widetilde{\Phi}^{(q^{(0)}=0)}$) and the values of $\{q_\lambda^{(0)}\}$.

Next, we consider the case where the shape of the unit cell is distorted from the reference structure. If the atom at $\mathbf{x}$ is moved to $\mathbf{X}$ by the deformation, the strain can be described by the displacement gradient tensor

$$u_{\mu\nu} = \frac{\partial X_\mu}{\partial x_\nu} - \delta_{\mu\nu}. \tag{12}$$

Under this strain, the atom α in the primitive cell $\mathbf{R}$ is shifted by

$$u_{\mathbf{R}\alpha\mu}^{(0)} = \sum_\nu u_{\mu\nu}(R_\nu + d_{\alpha\nu})$$
$$= \sum_\nu u_{\mu\nu}R_{\alpha\nu}, \tag{13}$$

in real space. $\mathbf{d}_\alpha$ is the atomic position of atom α in the primitive cell, and we define $\mathbf{R}_\alpha = \mathbf{R} + \mathbf{d}_\alpha$ for notational simplicity. Equation (13) expresses the strain by the shifts of constituting atoms. Following the same procedure as that for the change of internal coordinates, we can derive the formulas of the IFC renormalization for deformations of the primitive cell.

$$\hat{U}_n^{(u_{\mu\nu})} = \frac{1}{n!} \sum_{\{\mathbf{R}\alpha\mu\}} \Phi_{\mu_1\cdots\mu_n}^{(u_{\mu\nu})}(\mathbf{R}_1\alpha_1, \cdots, \mathbf{R}_n\alpha_n)\hat{u}_{\mathbf{R}_1\alpha_1\mu_1} \cdots \hat{u}_{\mathbf{R}_n\alpha_n\mu_n}, \tag{14}$$

$$\Phi_{\mu_1\cdots\mu_n}^{(u_{\mu\nu})}(\mathbf{R}_1\alpha_1, \cdots, \mathbf{R}_n\alpha_n)$$
$$= \sum_{m=0}^{\infty} \frac{1}{m!} \sum_{\{\mathbf{R}'\alpha'\mu'\nu'\}}$$
$$\times \Phi_{\mu_1\cdots\mu_n\mu_1'\cdots\mu_m'}^{(u_{\mu\nu}=0)}(\mathbf{R}_1\alpha_1, \cdots, \mathbf{R}_n\alpha_n, \mathbf{R}_1'\alpha_1', \cdots, \mathbf{R}_m'\alpha_m')$$
$$\times u_{\mu_1'\nu_1'}R_{1\alpha_1'\nu_1'}' \cdots u_{\mu_m'\nu_m'}R_{m\alpha_m'\nu_m'}'. \tag{15}$$

Combining Eqs. (11) and (15), it is possible to calculate the IFCs for arbitrary crystal structures ($\Phi^{(q^{(0)},u_{\mu\nu})}$ or $\widetilde{\Phi}^{(q^{(0)},u_{\mu\nu})}$) as long as the structural change is reasonably small. These equations are the key to the efficiency of our methods, which enables us to run SCP calculations without running additional DFT calculations at each structure optimization step.

We found that the second-order IFC renormalization by cell deformation [Eq. (15)] appears to be less accurate than that by atomic shift [Eq. (11)]. The former attempts to estimate the IFCs in the distorted unit cell which is different from the original one, but the atomic forces in the distorted cell are not included in the training data set used for extracting the original IFCs. By contrast, the latter changes the center of the Taylor expansion without changing the functional form of the potential energy surface. Hence, we provide an alternative option that directly calculates the coupling between the strain and the harmonic IFCs

$$\frac{\partial \Phi_{\mu_1\mu_2}(\mathbf{R}_1\alpha_1, \mathbf{R}_2\alpha_2)}{\partial u_{\mu\nu}}, \tag{16}$$

by finite displacement method in terms of the tensor $u_{\mu\nu}$, which we use in the calculation of BaTiO$_3$. This option ensures the accurate renormalization on the harmonic IFCs, which is vital to the quantitative description of structural phase transitions because the harmonic IFCs describe the stability/instability of the system. The additional computational cost is marginal compared to that for calculating the anharmonic IFCs. The details of the method to calculate the IFCs are described in Section III A. Hereafter in this paper, Φ and $\widetilde{\Phi}$ without notes on $q^{(0)}$ and $u_{\mu\nu}$ in superscripts signifies $\Phi^{(q^{(0)},u_{\mu\nu})}$ and $\widetilde{\Phi}^{(q^{(0)},u_{\mu\nu})}$ respectively, unless stated otherwise.

C. Structural optimization based on the SCP theory

In SCP theory, the SCP frequency $\Omega_{\boldsymbol{k}\lambda'}$ and the SCP polarization vectors are obtained by solving the SCP equation

$$
\begin{aligned}
\Omega^2_{\boldsymbol{k}\lambda_1\lambda_2} &= \sum_{n=1}^{\infty} \frac{1}{(n-1)! N^{n-1}} \sum_{\{\boldsymbol{k}\lambda'\}} \left(\frac{\hbar}{2}\right)^{n-1} \\
&\quad \frac{\widetilde{\Phi}(-\boldsymbol{k}\lambda_1, \boldsymbol{k}\lambda_2, \boldsymbol{k}_1\lambda'_1, -\boldsymbol{k}_1\lambda'_1, \cdots, -\boldsymbol{k}_{n-1}\lambda'_{n-1})}{\Omega_{\boldsymbol{k}_1\lambda'_1} \cdots \Omega_{\boldsymbol{k}_{n-1}\lambda'_{n-1}}} \\
&\quad \times \left(n_B(\hbar\Omega_{\boldsymbol{k}_1\lambda'_1}) + \frac{1}{2}\right) \cdots \left(n_B(\hbar\Omega_{\boldsymbol{k}_{n-1}\lambda'_{n-1}}) + \frac{1}{2}\right).
\end{aligned}
\tag{17}
$$

Here, $n_B(\hbar\Omega) = [e^{\beta\hbar\Omega} - 1]^{-1}$ is the Bose-Einstein distribution function, and $\beta = 1/k_B T$ is the inverse temperature with k_B being the Boltzmann constant. Note that indices of phonon modes with primes such as λ' denotes the updated modes, which diagonalizes the SCP dynamical matrix $\Omega_{\boldsymbol{k}\lambda_1\lambda_2}$ at temperature T. The phonon modes without primes like λ are fixed throughout the calculation. The SCP frequencies $\Omega_{\boldsymbol{k}\lambda'}$ are obtained by diagonalizing the SCP dynamical matrix as $\sum_{\lambda_1} \Omega_{\boldsymbol{k}\lambda\lambda_1} C_{\boldsymbol{k}\lambda_1\lambda'} = \Omega_{\boldsymbol{k}\lambda'} C_{\boldsymbol{k}\lambda\lambda'}$ using the C matrix, which is defined in Appendix A. See Appendix A for the detailed derivation of SCP equation. Because the derivation relies on the variational principle, the solution of the SCP equation [Eq. (17)] satisfies

$$
\frac{\partial \mathcal{F}}{\partial \Omega_{\boldsymbol{k}\lambda_1\lambda_2}} = 0,
\tag{18}
$$

for the variational free energy $\mathcal{F} = -k_B T \log \mathrm{Tr}\, e^{-\beta\hat{\mathcal{H}}_0} + \langle \hat{H} - \hat{\mathcal{H}}_0 \rangle_{\hat{\mathcal{H}}_0}$. Therefore, the gradient of the SCP free energy with respect to the atomic shift is calculated as

$$
\begin{aligned}
&\frac{1}{N} \frac{\partial \mathcal{F}(\widetilde{\Phi}^{(q^{(0)}, u_{\mu\nu})}, \Omega_{\boldsymbol{k}\lambda_1\lambda_2}(q^{(0)}, u_{\mu\nu}))}{\partial q_\lambda^{(0)}} \\
&= \frac{1}{N} \frac{\partial \mathcal{F}(\widetilde{\Phi}^{(q^{(0)}, u_{\mu\nu})}, \Omega_{\boldsymbol{k}\lambda_1\lambda_2})}{\partial q_\lambda^{(0)}} + \frac{1}{N} \sum_{\boldsymbol{k}\lambda_1\lambda_2} \frac{\partial \mathcal{F}}{\partial \Omega_{\boldsymbol{k}\lambda_1\lambda_2}} \frac{\partial \Omega_{\boldsymbol{k}\lambda_1\lambda_2}}{\partial q_\lambda^{(0)}} \\
&= \frac{1}{N} \frac{\partial \mathcal{F}(\widetilde{\Phi}^{(q^{(0)}, u_{\mu\nu})}, \Omega_{\boldsymbol{k}\lambda_1\lambda_2})}{\partial q_\lambda^{(0)}} \\
&= \sum_{n=0}^{\infty} \frac{1}{n! N^n} \sum_{\{\boldsymbol{k}\lambda\}} \left(\frac{\hbar}{2}\right)^n \frac{\widetilde{\Phi}(\boldsymbol{k}_1\lambda'_1, -\boldsymbol{k}_1\lambda'_1, \cdots, \boldsymbol{k}_n\lambda'_n, -\boldsymbol{k}_n\lambda'_n, 0\lambda)}{\Omega_{\boldsymbol{k}_1\lambda'_1} \cdots \Omega_{\boldsymbol{k}_n\lambda'_n}} \\
&\quad \times \left(n_B(\hbar\Omega_{\boldsymbol{k}_1\lambda'_1}) + \frac{1}{2}\right) \cdots \left(n_B(\hbar\Omega_{\boldsymbol{k}_n\lambda'_n}) + \frac{1}{2}\right),
\end{aligned}
\tag{19}
$$

in the normal coordinate representation, where we used Eqs. (11) and (A5). $\Omega_{\boldsymbol{k}\lambda_1\lambda_2}(q_\lambda^{(0)}, u_{\mu\nu})$ is the solution of the SCP equation for the crystal structure given by $q_\lambda^{(0)}$, $u_{\mu\nu}$. As for the cell deformation, the gradient of the SCP free energy with respect to the displacement gradient tensor $u_{\mu\nu}$ can be derived in the same way. Here, we add the pV term to the free energy

to take into account the effect of pressure.

$$
\begin{aligned}
&\frac{1}{N} \frac{\partial \mathcal{F}(\widetilde{\Phi}^{(q^{(0)}, u_{\mu\nu})}, \Omega_{\boldsymbol{k}\lambda_1\lambda_2}(q^{(0)}, u_{\mu\nu}))}{\partial u_{\mu\nu}} \\
&= \frac{1}{N} \frac{\partial \mathcal{F}(\widetilde{\Phi}^{(q^{(0)}, u_{\mu\nu})}, \Omega_{\boldsymbol{k}\lambda_1\lambda_2})}{\partial u_{\mu\nu}} \\
&= p \frac{\partial v_{\mathrm{cell}}}{\partial u_{\mu\nu}} \\
&\quad + \sum_{n=0}^{\infty} \frac{1}{n! N^n} \sum_{\{\boldsymbol{k}\lambda\}} \left(\frac{\hbar}{2}\right)^n \frac{\partial \widetilde{\Phi}(\boldsymbol{k}_1\lambda'_1, -\boldsymbol{k}_1\lambda'_1, \cdots, \boldsymbol{k}_n\lambda'_n, -\boldsymbol{k}_n\lambda'_n)}{\partial u_{\mu\nu}} \\
&\quad \times \frac{(n_B(\hbar\Omega_{\boldsymbol{k}_1\lambda'_1}) + 1/2)}{\Omega_{\boldsymbol{k}_1\lambda'_1}} \cdots \frac{(n_B(\hbar\Omega_{\boldsymbol{k}_n\lambda'_n}) + 1/2)}{\Omega_{\boldsymbol{k}_n\lambda'_n}},
\end{aligned}
\tag{20}
$$

where p is the static pressure and v_{cell} is the volume of the unit cell. Using the above formulas, we can relax the crystal structure to minimize the SCP free energy in the following way. Concerning the internal coordinates, the difference $\delta q_\lambda^{(0)}$ from the optimum values at a given temperature can be estimated by solving

$$
\frac{1}{N} \frac{\partial \mathcal{F}}{\partial q_\lambda^{(0)}} = \sum_{\lambda_1} \Omega_{0\lambda\lambda_1} \delta q_{\lambda_1}^{(0)},
\tag{21}
$$

if we approximate the Hessian of the SCP free energy by the SCP dynamical matrix $\Omega_{0\lambda_1\lambda_2}$. The internal coordinate is updated as

$$
q_\lambda^{(0)} \leftarrow q_\lambda^{(0)} - \beta_{\mathrm{mix,ion}} \delta q_\lambda^{(0)}.
\tag{22}
$$

$\beta_{\mathrm{mix,ion}}$ is introduced to make the calculation scheme more robust and is usually chosen to be $0 < \beta_{\mathrm{mix,ion}} < 1$. In updating the shape of the unit cell, we estimate the difference $\delta u_{\mu\nu}$ from the optimum value by

$$
\frac{1}{N} \frac{\partial \mathcal{F}}{\partial u_{\mu\nu}} = \sum_{\mu_1\nu_1} C_{\mu\nu, \mu_1\nu_1} \delta u_{\mu_1\nu_1},
\tag{23}
$$

where we approximate the Hessian of the SCP free energy by the second-order elastic constants $C_{\mu\nu, \mu_1\nu_1}$, which is defined in Appendix C. We restrict the solution $\delta u_{\mu_1\nu_1}$ of Eq. (23) to be symmetric in order to fix the rotational degree of freedom and get an unique solution. The displacement gradient tensor is updated by

$$
u_{\mu\nu} \leftarrow u_{\mu\nu} - \beta_{\mathrm{mix,cell}} \delta u_{\mu\nu},
\tag{24}
$$

where $0 < \beta_{\mathrm{mix,cell}} < 1$ is a coefficient like $\beta_{\mathrm{mix,ion}}$, which is introduced to improve robustness of the calculation.

Putting together the above considerations, the calculation scheme of the structural optimization based on SCP theory is as follows, which is visualized with a flowchart in Fig. 1.

1. Calculate IFCs of the current structure by the IFC renormalization.

2. Solve SCP equation (Eq. (A19))

3. Calculate the gradient of the SCP free energy by Eqs. (19) and (20).

4. Update crystal structure by Eqs. (22) and (24).

5. Check convergence. The calculation ends if the converged structure has been obtained.

6. If convergence has not been achieved, return to 1.

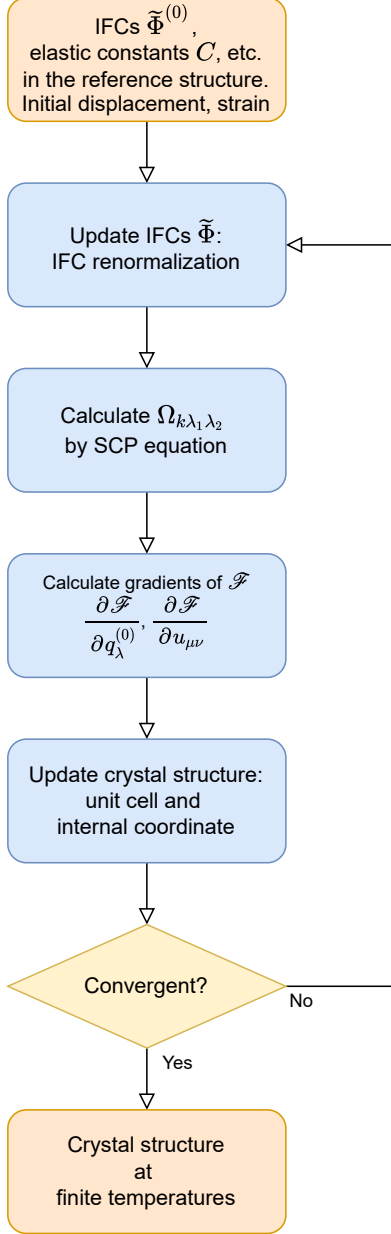We discuss the details of the implementation in Appendix C.

FIG. 1. Schematic figure of the calculation flow of the structural optimization at finite temperature based on SCP theory.

III. SIMULATION DETAILS

We apply the developed method to the thermal expansion of silicon and the three-step structural phase transition of BaTiO$_3$. In this section, we describe the detailed setting in the calculation of these materials.

A. Calculation of the interatomic force constants (IFCs) and the SCP calculation

The interatomic force constants (IFCs) and the elastic constants are calculated before performing the structural optimization at finite temperatures. The Taylor expansion of the potential energy surface is truncated at the fourth-order ($\hat{U} \simeq U_0 + \hat{U}_2 + \hat{U}_3 + \hat{U}_4$). The IFCs are calculated by fitting the relationship between atomic displacements and atomic forces, which are calculated by using external DFT packages. The fitting is performed by the compressive sensing method, which enables the efficient extraction of IFCs from a small number of displacement-force data [37, 61, 62]. We impose on the IFCs the acoustic sum rule, the permutation symmetry, and the space group symmetry not only in the supercell model but also in the infinite real space. The details on the sum rules and symmetries of the IFCs are described in Appendix D. The second-order and third-order elastic constants are calculated by fitting the strain-energy relation making use of the crystal symmetry [63, 64].

For silicon, 2×2×2 conventional cubic supercell, which contains 64 atoms, is used in the phonon calculation. We use the lattice constant 5.4362 Å for calculating the IFCs and the elastic constants, which is obtained by the structural optimization based on DFT so that the stress tensor in the reference structure vanishes. We generate 100 configurations by the random sampling at 300 K from harmonic phonon dispersion to obtain the displacement-force data and extract the anharmonic IFCs. The cutoff radius, which is introduced in Appendix F, for the third and fourth-order IFCs are 20.0 Bohr and 10.0 Bohr, respectively. The cutoff radius for the fourth-order IFCs can be relatively small because the anharmonicity is so weak in silicon that the higher-order IFCs are highly localized. The fitting error of the displacement-force data is 0.52 %. We use $8 \times 8 \times 8$ k-mesh for the SCP calculation.

A 2×2×2 supercell, which contains 40 atoms, is employed for the phonon calculation of BaTiO$_3$. The high-symmetry cubic cell with the lattice constant 3.9855 Å is employed as the reference structure, which is used to calculate IFCs and the elastic constants, whose lattice constant is obtained by the DFT-based structural optimization. We choose the cubic phase as the reference structure to take full advantage of the crystal symmetry. For BaTiO$_3$, we generated 300 configurations by adding random displacements to AIMD snapshots. The AIMD calculation is run with a smaller basis cutoff and a smaller number of k-points to efficiently sample the potential energy surface, whose details are shown in the next section. The displacement-force data are generated by DFT calculations with higher accuracy. We set the cutoff radius for the third and fourth-order IFCs as 15.0 Bohr, which is compara-

ble to one side of the supercell. The fourth-order IFCs are restricted up to three-body terms, in which at least two of the four atoms regarding the IFC are the same. The fitting error of the forces is 3.51 %, which shows that the calculated IFCs well reproduce the complex landscape of the potential energy surface of $BaTiO_3$. We use $8 \times 8 \times 8$ k-mesh and do not add the nonanalytic correction to the dynamical matrix in the SCP calculation. The convergence of the calculation results with respect to the setting in the IFC calculation and the SCP calculation are thoroughly checked in Appendices F~J.

B. DFT calculation

We employ the *Vienna ab initio simulation package* (VASP) [27] for the electronic structure calculations. The PBEsol exchange-correlation functional [65] and the PAW pseudopotentials [66, 67] are used. The convergence criteria of the SCF loop is set 10^{-8} eV and accurate precision mode, which suppresses egg-box effects and errors, are used to calculate the forces accurately. We use a $4 \times 4 \times 4$ Monkhorst-Pack k-mesh for both materials. The basis cutoff is set 500 eV for silicon and 600 eV for $BaTiO_3$. A $2 \times 2 \times 2$ Monkhorst-Pack k-mesh and basis cutoff of 400 eV are used for the AIMD calculation of $BaTiO_3$, which is for sampling the potential energy surface to generate the random configurations.

IV. RESULT AND DISCUSSION

We perform the first-principles calculation on the thermal expansion of silicon and the successive structural phase transitions of $BaTiO_3$.

A. Silicon

The thermal expansion of silicon is calculated by the structural optimization at finite temperatures developed in this research. Since the internal coordinate in the cubic cell is determined by the symmetry, only the lattice constant a change with temperature. In Fig. 2, the linear thermal expansion coefficient $\alpha_L = \frac{1}{a}\frac{\partial a}{\partial T}$ calculated by two methods are compared, where a is the lattice constant. In the former method (SCP, IFCs from DFT at each a), the calculation of the IFCs and the free energy is performed at 14 different lattice constants, and the optimum lattice constant at each temperature is obtained by fitting the free energy by the Birch-Murnaghan equation of state [68, 69], as in the calculations in Refs. [57, 70]. It is more accurate because the IFCs are calculated from DFT calculations at different lattice constants instead of estimating them by the IFC renormalization. However, our method (SCP, renormalized IFCs) is much more efficient than the other because running the DFT calculations to generate the displacement-force data is the most expensive part of the calculation. The calculation results of the two methods in Fig. 2 are almost identical, which confirms that the IFC renormalization accurately calculates the change of IFCs in this case. The accuracy of

the IFC renormalization is also tested in Appendix E by investigating the harmonic phonon dispersions in different lattice constants.
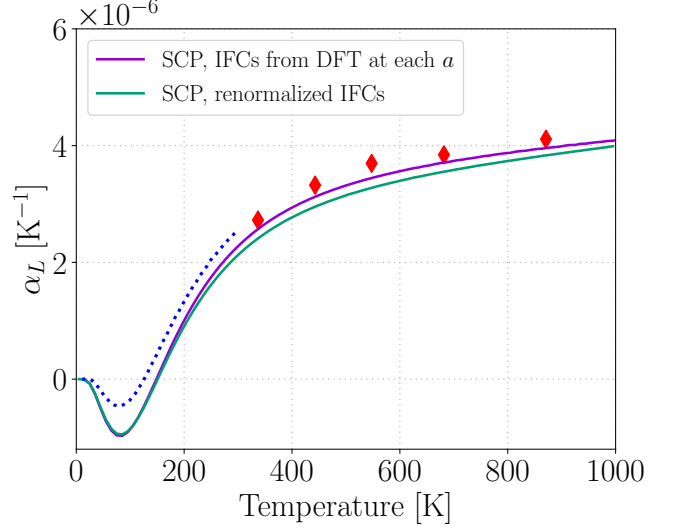

FIG. 2. Calculation results of the temperature dependence of the linear thermal expansion coefficient $\alpha_L = \frac{1}{a}\frac{\partial a}{\partial T}$, where a is the lattice constant. In the calculation of the purple line (SCP, IFCs from DFT at each a), the calculation of the IFCs and the free energy is performed at 14 different lattice constants and the optimum lattice constant at each temperature is obtained by fitting the free energy by the Birch-Murnaghan equation of state. For the green line (SCP, renormalized IFCs), the lattice constant is directly calculated by the structural optimization at finite temperature including the nuclear quantum effect, which is developed in this research. The experimental data are taken from Ref. [71] (blue dotted line) and Ref. [72] (red diamond).

B. BaTiO3

1. Structural optimization at finite temperatures

$BaTiO_3$ is a typical perovskite ferroelectrics, which shows a three-step structural phase transition at ambient pressure [2, 13, 41, 45, 73, 74]. When the temperature is lowered, it exhibits structural phase transitions from the cubic phase to the tetragonal phase at around 390 K, then to the orthorhombic phase at around 270 K, and lastly to the rhombohedral phase at around 180 K [13].

We start with the calculation at ambient pressure, where we set the static pressure as 0 GPa. We first calculate the cubic-tetragonal phase transition, which occurs at the highest temperature of the three structural phase transitions. The temperature dependence of the crystal structure (displacement gradient tensor $u_{\mu\nu}$ and the atomic displacements $u_{\alpha z}^{(0)}$) is shown in Fig. 3. In the cooling calculation, the initial structure is set by adding a small displacement to the high-symmetry cubic phase to induce symmetry breaking. In the heating calculation, we start

from the lower temperatures and use the optimized structure at the previous temperature as the initial structure for the calculation at each temperature. According to the figure, the atomic displacements are zero at high temperature while they become finite at low temperature, which shows the presence of the structural phase transition. The hysteresis between the cooling and heating calculations shows that the transition is first-order, which is consistent with the experiments although its temperature range is overestimated [2, 13].
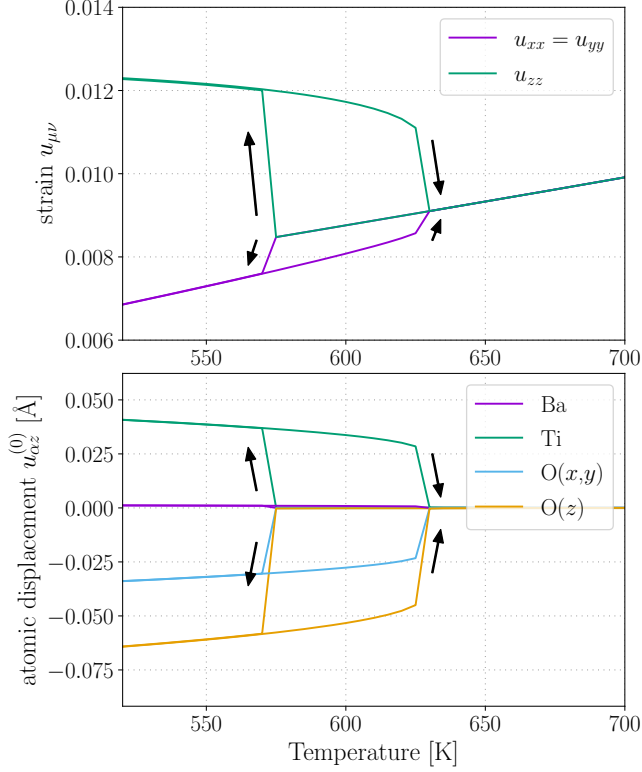
FIG. 3. Temperature dependence of the crystal structure near the cubic-tetragonal phase transition of BaTiO$_3$. A hysteresis is observed between the cooling and heating calculations. In the cooling calculation, the initial structure is set by adding a small displacement to the high-symmetry cubic phase to induce symmetry breaking. In the heating calculation, we start from the lower temperatures and use the optimized structure at the previous temperature as the initial structure for the calculation at each temperature. Both the unit cell and internal coordinates are relaxed considering the nuclear quantum effect.

Figure 4 depicts the calculation result of the T-dependent SCP free energy of the four phases of BaTiO$_3$. As shown in Fig. 4, the cubic phase is the most stable at high temperatures. As the temperature is lowered, the tetragonal phase, the orthorhombic phase, and then the rhombohedral phase become the most stable, whose order is consistent with the experiment. Therefore, we have successfully reproduced the three-step structural phase transition of BaTiO$_3$ with our method. The transition temperatures (T_c) can be calculated from the crossing points of the free energy, which are comparable to the experimental results as summarized in Table I. The origin

TABLE I. Transition temperatures of the three successive structural phase transitions of BaTiO$_3$. The comparison between the calculation results estimated from the crossing points of the SCP free energy and the experimental result [2]. The nuclear quantum effect is taken into account in the calculation.

	our method [K]	experiment [K]
cubic-tetra	606	~390
tetra-ortho	509	~270
ortho-rhombo	411	~180

of the differences between the experimental and calculation results are discussed later in this section in relation to the lattice constants.
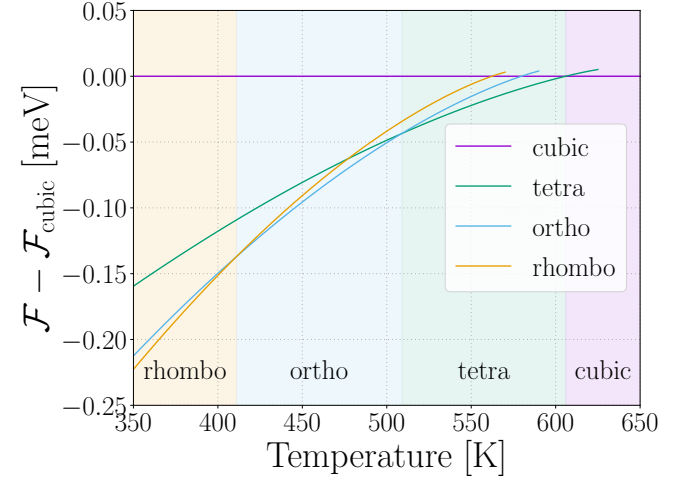

FIG. 4. Temperature-dependence of SCP free energy of the four phases of BaTiO$_3$ calculated by the structural optimization at finite temperature. The difference from the SCP free energy of the cubic phase $\mathcal{F}_{\text{cubic}}$ is plotted to make the difference clearer. The nuclear quantum effect is included in the calculation of the crystal structure and the free energy.

The calculation results of the lattice constants and the spontaneous polarization are shown in Fig. 5 and 6, which are in agreement with the experimental results [2] if the difference in transition temperatures are compensated. The spontaneous polarization is calculated by using the atomic displacements $u_{\alpha\nu}^{(0)}$ and the Born effective charge $Z_{\alpha,\mu\nu}^*$ as

$$P_\mu = \frac{e}{V_{\text{cell}}} \sum_{\alpha\nu} Z_{\alpha,\mu\nu}^* u_{\alpha\nu}^{(0)}, \tag{25}$$

where V_{cell} is the volume of the primitive cell and e is the elementary charge. The Born effective charge is calculated by density functional perturbation theory [75, 76] in the original high-symmetry cubic structure. In Figs. 5 and 6, we show the hysteresis only for the cubic-tetragonal phase transition since we have not directly calculated the transitions between the tetragonal and the orthorhombic phase and between the orthorhombic and the rhombohedral phases. This is because

we calculate the phase transitions between the cubic phase and each of the other three phases to take full advantage of the crystal symmetry.

Let us discuss the origin of the overestimation of T_c in Table I. The lattice constant is one of the primary factors that produce this deviation. In the inset in Fig. 7 (a), we show the relation between the calculated T_c of the cubic-tetragonal phase transition in BaTiO$_3$ and the lattice constant a at the corresponding temperature, which is derived from the finite-pressure calculations. The transition temperature at the experimental value of $a = 4.0093$ Å is estimated as 511 K from the linear fitting in the figure. Thus, the error in the lattice constant explains around half of the error in the transition temperature. The other possible sources of the errors in the transition temperatures can be the error in the DFT functional, the truncation of the Taylor expansion of the potential energy surface at the fourth order, and the approximation of the SCP theory.

The error in the lattice constant originates from the errors of the functional used in the DFT calculations. From the inset of Fig. 7 (a), we estimate that $\frac{dT_c}{da} \sim 8500$ K Å^{-1}. Since the PBEsol functional predicts the lattice constants of materials with the accuracy of 0.3 % [77], the DFT error of the lattice constant can lead to an error in T_c of around 102 K in this case. Comparing at the same temperature, the error of the lattice constant in our calculation is around 0.2 %, which is within the DFT accuracy but significantly affects the calculated transition temperature.

We then investigate the pressure dependence of transition temperatures to draw the p-T phase diagram of BaTiO$_3$. Similar calculations are run with different pressures, and the pressure (p)-dependent transition temperatures are estimated either from the crossing points of the T-dependent free energies or from the onset of finite atomic displacements when no hysteresis is observed between the cooling and the heating calculations. The resultant phase diagram is shown in Fig. 7. The calculated phase diagram well reproduces the experimental result [78]. At zero temperature, the rhombohedral phase is the most stable at low pressure. Applying the pressure, the orthorhombic phase, tetragonal phase, and then the cubic phase become the most stable, which is shown to be a consequence of the nuclear quantum effect [41].

Note that the temperature dependences of the crystal structures in Figs. 3~6 are calculated at every 5 K, and the gaps are connected by linear interpolation. The plotted curves look smooth because we perform a deterministic calculation on a fine temperature grid. This is because we do not need to run time-consuming electronic structure calculations at each temperature or structural optimization step, which is enabled by the IFC renormalization as discussed in Section II B. Therefore, the most costly part of the calculation is to run electronic structure calculations to get the force-displacement data for the 300 supercells. In comparison, the computational cost of each step of the structural optimization is negligible, which is one of the most significant advantages of the present method compared to other methods [36, 52–54]. In addition, this property is also effective in the calculation of p-T phase diagram in Fig. 7 because no additional electronic structure calculations are required for calculations at different pressures.
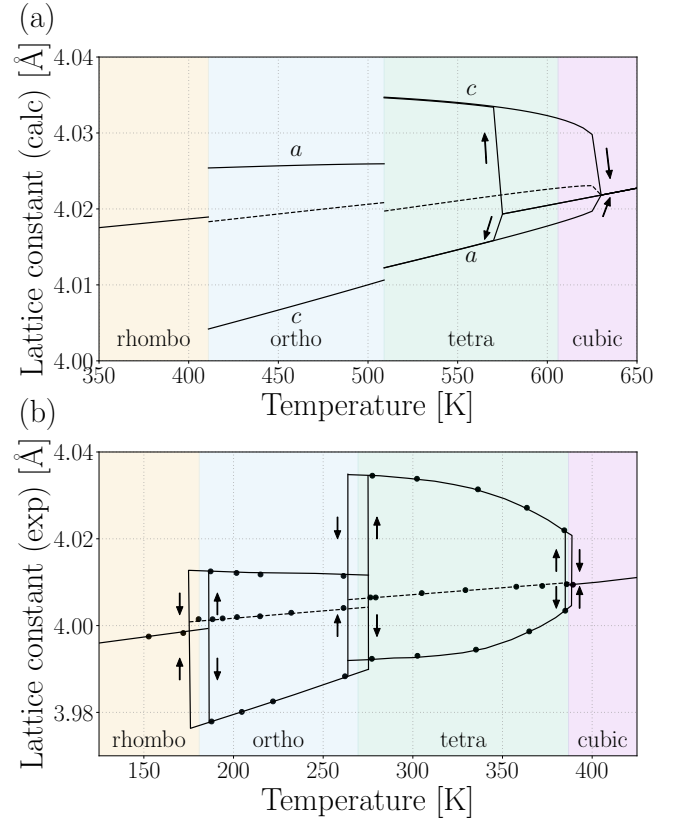

FIG. 5. (a) Calculation result of the temperature-dependent lattice constants of BaTiO$_3$. The results of the rhombohedral and the orthorhombic phases are plotted only in the temperature ranges where each phase is the most stable. The dotted lines represent the cubic root of the cell volume. The hysteresis between the cooling and the heating calculations is plotted for the cubic-tetragonal phase transition. Both the unit cell and internal coordinates are relaxed including the nuclear quantum effect. (b) The experimental data taken from Ref. [2]. The boundaries of the background colors of each phase are taken to be the center of the hysteresis regions.

Some works proposed that the phase transitions of BaTiO$_3$ have an order-disorder nature [45, 79–81], which is characterized by multiple-peak distribution of atomic positions above T_c. Our method based on SCP theory does not reproduce this property because the distribution is calculated within the effective harmonic Hamiltonian. However, softening of the optical phonons is observed in BaTiO$_3$ [82, 83], which indicates that the treatment using the effective harmonic Hamiltonian is valid in this material. Since the main point of SCP theory is to calculate the best effective harmonic Hamiltonian by the variational principle, we consider that the SCP theory can be applied when the effective harmonic approach is reasonable, which is supported by the calculation results. Even when the transition is order-disorder or mixed type, SCP theory captures the general trend of the true distribution in a mean-field way because the displacement along the soft mode will be larger near the phase transition.
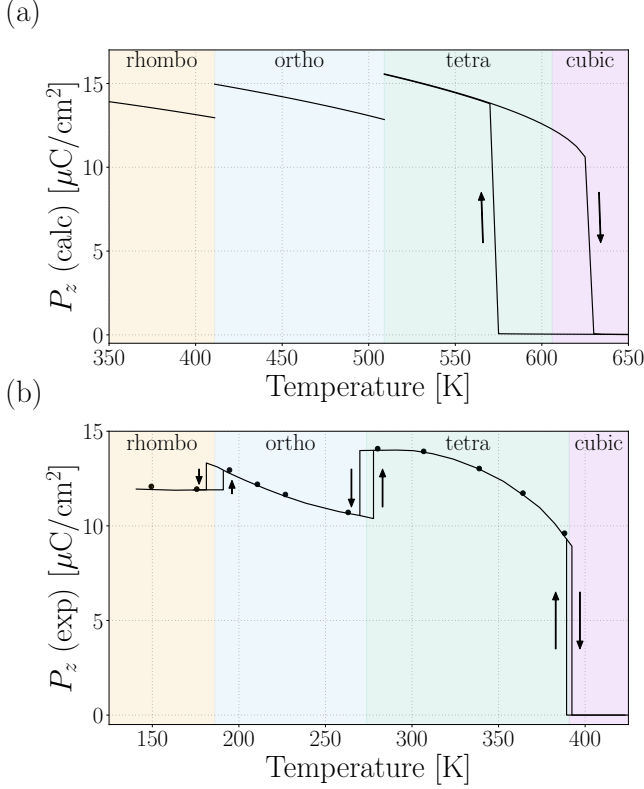
(a)

(b)

FIG. 6. (a) Calculation result of the temperature dependence of the spontaneous polarization P_z. The results of the rhombohedral and the orthorhombic phase are plotted only in the temperature ranges where each phase is the most stable. The hysteresis between the cooling and the heating calculations is plotted for the cubic-tetragonal phase transition. The spontaneous polarization is calculated from the atomic displacements and the Born effective charge. Both the unit cell and internal coordinates are relaxed including the nuclear quantum effect. (b) The experimental data taken from Ref. [2]. The boundaries of the background colors of each phase are taken to be the center of the hysteresis regions.

2. Importance of relaxing the shape of the unit cell

We perform the calculation of the structural phase transitions of $BaTiO_3$ with the unit cell fixed to the original cubic cell to investigate the importance of relaxing the unit cell. The calculation result of the free energy of the four phases is shown in Fig. 8. In Fig 8, the three transition temperatures are very close to each other, with gaps of around only 10 K. These gaps between transition temperatures are much smaller than in Fig. 4, in which calculation the unit cell is relaxed.

We consider that there are two possible reasons for the underestimation of the gaps between transition temperatures when the unit cell is fixed. Firstly, the stabilization effect by the cell deformation is underestimated in the tetragonal and orthorhombic phases. In both phases, the cell will get elongated to the polarization direction, which is in the z direction for the tetragonal phase and in the xy direction for the orthorhombic phase. This effect will be smaller in the cubic and the rhombo-
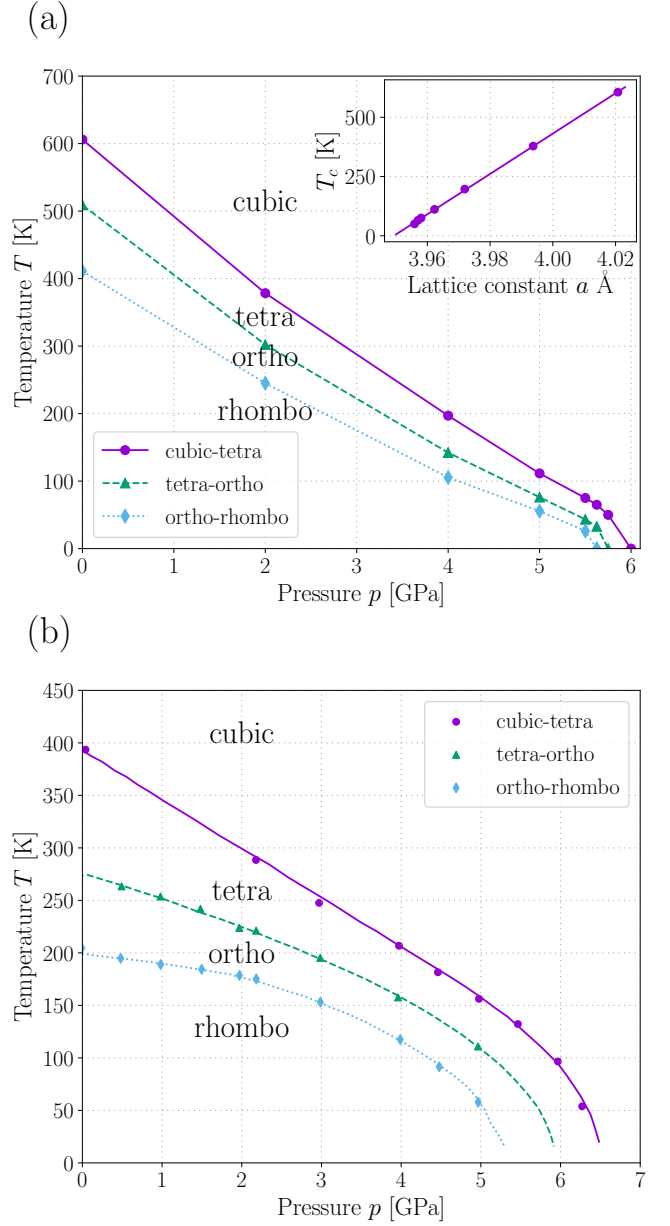
(a)

(b)

FIG. 7. (a) The p-T phase diagram of $BaTiO_3$ calculated by the structural optimization at finite temperature including the nuclear quantum effect. The inset shows the relation between the lattice constant a and the transition temperature T_c of the cubic-tetragonal phase transition. (b) The experimental result taken from Ref. [78].

hedral phase because the three lattice constants are the same as shown in Fig. 5. Therefore, if the unit cell is fixed, the crossing point of the free energy curves of the cubic and the tetragonal phase is shifted to a lower temperature while that of the orthorhombic and the rhombohedral phase is shifted to a higher temperature. The second possible explanation is the effect of thermal expansion. In general, the instability of the soft mode gets more significant if the unit cell expands, which can be seen from Figs. 13 and 14. Hence, the transition temperatures

will become higher in expanded unit cells. When the effect of thermal expansion is taken into account, the higher transition temperatures will go further higher than lower transition temperatures because high-symmetry phases become less favored in expanded cells. Therefore, it is vital to relax the shape of the unit cell to perform accurate calculations on the structural phase transition of materials, especially when three or more competing phases are involved.
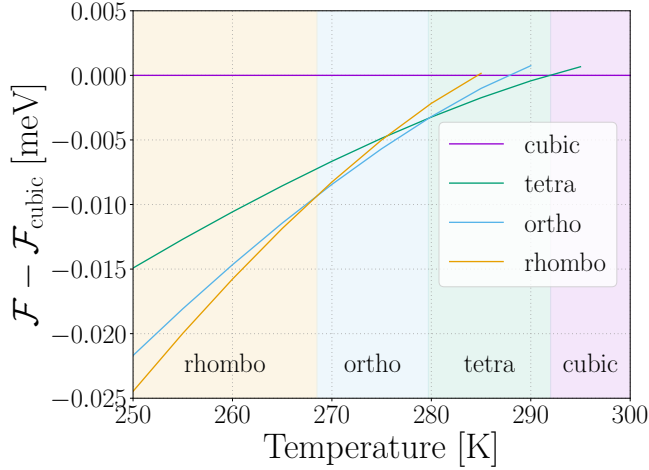

FIG. 8. The temperature-dependence of SCP free energy of the four phases of BaTiO$_3$ calculated by the structural optimization at finite temperature. The unit cell is fixed to the original cubic cell and only the internal coordinates are relaxed. The difference from the SCP free energy of the cubic phase $\mathcal{F}_{\text{cubic}}$ is plotted to make the difference clearer. The nuclear quantum effect is included in the calculation.

3. Significance of the nuclear quantum effect

We examine the importance of considering the nuclear quantum effect in calculating the structural phase transition. Here, we perform calculation without nuclear quantum effect, in which we replace $n_B(\hbar\omega) + \frac{1}{2}$ by $\frac{k_B T}{\hbar\omega}$ in the theory. The calculations are performed for four different phases of BaTiO$_3$, and the T-dependent crystal structure and free energy are calculated. The three-step structural phase transition of BaTiO$_3$ has been reproduced by the calculation without nuclear quantum effect. However, as shown in Table II, the transition temperatures are overestimated when we disregard the nuclear quantum effect. This overestimation occurs because the quantum fluctuation stabilizes the high-symmetry phases.

In addition, the temperature dependence of the spontaneous polarization and the crystal structure near the cubic-tetragonal phase transition are shown in Figs. 9 and 10. We can see that the spontaneous polarization is overestimated compared to the experimental results or the calculation that includes the nuclear quantum effect, which are shown in Fig. 5. According to Fig. 10, the deviation from the cubic structure gets larger in the classical calculation, which we identify as the reason for the overestimation of spontaneous polarization P.

TABLE II. Transition temperatures of the successive structural phase transitions of BaTiO$_3$. The comparison between the calculation results with and without nuclear quantum effect (NQE). The calculation which considers the nuclear quantum effect is explained in Section IV B in the main part. [2].

	with NQE [K]	without NQE [K]
cubic-tetra	606	666
tetra-ortho	509	572
ortho-rhombo	411	475

From the above analysis, we can see that the nuclear quantum effect has a significant impact on the crystal structures near the structural phase transitions, and properly incorporating it is essential for the quantitative prediction of material properties at finite temperatures.
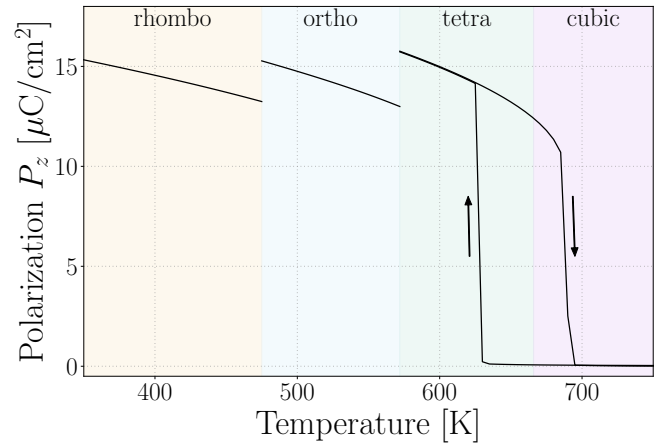

FIG. 9. Temperature dependence of the spontaneous polarization P_z calculated without nuclear quantum effect. The results of the rhombohedral and the orthorhombic phase are plotted only in the temperature ranges where each phase is the most stable. The hysteresis between the cooling and the heating calculations is plotted for the cubic-tetragonal phase transition. The spontaneous polarization is calculated from the atomic displacements and the Born effective charge as in Eq. (25).

V. CONCLUSION

We formulate the theory of structural optimization at finite temperature based on the SCP theory, which can accurately describe the lattice vibrations with strong anharmonic effect. The crystal structure is calculated by minimizing the SCP free energy with the help of its gradient with respect to the internal coordinates and the displacement gradient tensor $u_{\mu\nu}$. The interatomic force constants are updated without additional DFT calculations at each structural optimization step, which makes the calculation efficient.

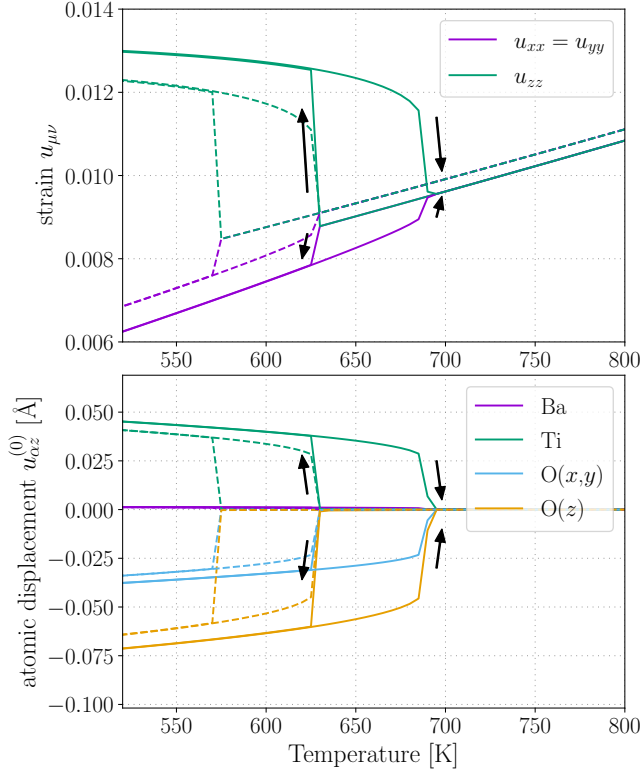We implement the theory to the ALAMODE package [37, 55, 57] and perform calculations on silicon and BaTiO$_3$, which

FIG. 10. Temperature dependence of the crystal structure near the cubic-tetragonal phase transition of BaTiO₃. The solid represents the calculation without nuclear quantum effect. The dashed line is the calculation results with nuclear quantum effect, which is plotted for comparison.

accurately reproduce the experimental results. As for BaTiO₃, we have successfully reproduced its three-step structural phase transition with quantitative agreement between theory and experiment for the T-dependent lattice constants and spontaneous polarization. Furthermore, the pressure-temperature (p-T) phase diagram of BaTiO₃ calculated by the developed method shows good agreement with experiment.

The present methodology can be generally applied to a wide range of materials. We expect that it lays the foundation for the non-empirical calculation of exotic finite temperature properties near the structural phase transitions.

Appendix A: Self-consistent phonon (SCP) theory

We derive the self-consistent phonon (SCP) equation in momentum-space representation from the variational principle of the free energy. The resultant SCP equation is equivalent to the previous derivations that use self-energy and Dyson's equation [37] or the ones in real-space representation [84]. The variational property plays an important role in calculating the gradient of the SCP free energy in Section II C.

In preparation, we define the C matrix, which describes the mode transformation, as

$$\hat{q}_{k\lambda} = \sum_{\lambda'} C_{k\lambda\lambda'} \hat{q}_{k\lambda'}, \qquad (A1)$$

$$C_{k\lambda\lambda'} = \sum_{\alpha\mu} \epsilon^*_{k\lambda,\alpha\mu} \epsilon_{k\lambda',\alpha\mu}, \qquad (A2)$$

where λ' is the index of the updated polarization vector and the λ of the original polarization vector. The updated mode λ' diagonalizes the SCP dynamical matrix like Eq. (A7). The original mode λ must be fixed throughout the structural optimization process, for which we take the mode that diagonalizes the harmonic dynamical matrix in the reference structure, $\widetilde{\Phi}^{(q^{(0)}=0, u_{\mu\nu}=0)}$. We distinguish the indices of the original mode and the updated mode by the absence and the presence of prime ($'$), as stated in Section II C.

The variational principle that the trial free energy $\mathcal{F}$ defined below are always the same or larger than the true free energy F, is used in the derivation of the SCP equation.

$$\mathcal{F} = -k_B T \log \text{Tr}\, e^{-\beta \hat{\mathcal{H}}_0} + \langle \hat{H} - \hat{\mathcal{H}}_0 \rangle_{\hat{\mathcal{H}}_0} \geq F. \qquad (A3)$$

Note that $\mathcal{F}$ and F need to include pV term when we consider systems under static pressure. However, we don't treat the pV term explicitly in this Appendix because it does not play an important role here. In SCP theory, we restrict the trial Hamiltonian $\hat{\mathcal{H}}_0$ to harmonic Hamiltonians

$$\hat{\mathcal{H}}_0 = \sum_{k\lambda'} \hbar \Omega_{k\lambda'} \hat{a}^\dagger_{k\lambda'} \hat{a}_{k\lambda'}. \qquad (A4)$$

The variational parameters $C_{k\lambda\lambda'}$ (or $\epsilon_{k\lambda',\alpha\mu}$) and $\Omega_{k\lambda'}$ are optimized so as to minimize the variational free energy to get the best approximation of the original problem. We first calculate the variational free energy by substituting Eq. (A4)

to Eq. (A3).

$$\mathcal{F} = -k_B T \log \text{Tr}\, e^{-\beta\hat{\mathcal{H}}_0} + \langle \hat{H} - \hat{\mathcal{H}}_0 \rangle_{\hat{\mathcal{H}}_0}$$

$$= \sum_{k\lambda'} \left[\frac{1}{2}\hbar\Omega_{k\lambda'} + k_B T \log\left(1 - e^{-\beta\hbar\Omega_{k\lambda'}}\right) \right]$$

$$- \sum_{k\lambda'} \frac{\hbar}{2}\left(n_B(\hbar\Omega_{k\lambda'}) + \frac{1}{2}\right)$$

$$\times \left(\Omega_{k\lambda'} - \sum_{\lambda_1\lambda_2} \frac{C^*_{k\lambda_1\lambda'}\widetilde{\Phi}(-k\lambda_1, k\lambda_2)C_{k\lambda_2\lambda'}}{\Omega_{k\lambda'}}\right)$$

$$+ \sum_{n=2}^{\infty} \frac{1}{n!}\frac{1}{N^{n-1}} \sum_{\{k\lambda'\}} \left(\frac{\hbar}{2}\right)^n \frac{\widetilde{\Phi}(k_1\lambda'_1, -k_1\lambda'_1, \cdots, k_n\lambda'_n, -k_n\lambda'_n)}{\Omega_{k_1\lambda'_1}\cdots\Omega_{k_n\lambda'_n}}$$

$$\times \left(n_B(\hbar\Omega_{k_1\lambda'_1}) + \frac{1}{2}\right)\cdots\left(n_B(\hbar\Omega_{k_n\lambda'_n}) + \frac{1}{2}\right). \tag{A5}$$

The IFCs in the updated-mode representation are defined as

$$\widetilde{\Phi}(k_1\lambda'_1, \cdots, k_m\lambda'_m)$$

$$= \sum_{\lambda_1\cdots\lambda_m} \widetilde{\Phi}(k_1\lambda_1, \cdots, k_m\lambda_m)C_{k_1\lambda_1\lambda'_1}\cdots C_{k_m\lambda_m\lambda'_m} \tag{A6}$$

Now, let us consider minimizing the variational free energy of Eq. (A5). We treat the SCP dynamical matrix

$$\Omega_{k\lambda_1\lambda_2} = \sum_{\lambda'} C_{k\lambda_1\lambda'}\Omega_{k\lambda'}C^*_{k\lambda_2\lambda'} \tag{A7}$$

as the variational parameters because the C matrix is difficult to handle due to the unitarity condition and the phase degrees of freedom. Abbreviating the momentum and the mode indices, the SCP dynamical matrix can be written as $\Omega = CDC^\dagger$, where $D = \text{diag}(\Omega_{k\lambda'})$. Here, we derive some formulas that are used in the following derivation of the SCP equation. We consider that the SCP dynamical matrix $\Omega = CDC^\dagger$ is dependent on a parameter s. From the unitarity of the C matrix, we can show

$$\frac{\partial C^\dagger}{\partial s}C + C^\dagger\frac{\partial C}{\partial s} = 0. \tag{A8}$$

Differentiating both hand sides of $\Omega = CDC^\dagger$, we get

$$\frac{\partial D}{\partial s} = C^\dagger\frac{\partial \Omega}{\partial s}C - C^\dagger\frac{\partial C}{\partial s}D - D\frac{\partial C^\dagger}{\partial s}C. \tag{A9}$$

The diagonal component in the update-mode representation is written as

$$\frac{\partial\Omega_{k\lambda'}}{\partial s} = \left(C^\dagger\frac{\partial\Omega}{\partial s}C\right)_{\lambda'\lambda'}. \tag{A10}$$

Thus, substituting $s = \Omega_{k\lambda_1\lambda_2}$, we get

$$\frac{\partial\Omega_{k\lambda'}}{\partial\Omega_{k\lambda_1\lambda_2}} = C^*_{k\lambda_1\lambda'}C_{k\lambda_2\lambda'}. \tag{A11}$$

We also consider the off-diagonal components:

$$\left(C^\dagger\frac{\partial\Omega}{\partial s}C\right)_{\lambda'_1\lambda'_2} = \left(C^\dagger\frac{\partial C}{\partial s}\right)_{\lambda'_1\lambda'_2}\Omega_{k\lambda'_2} + \Omega_{k\lambda'_1}\left(\frac{\partial C^\dagger}{\partial s}C\right)_{\lambda'_1\lambda'_2} \tag{A12}$$

$$= (\Omega_{k\lambda'_2} - \Omega_{k\lambda'_1})\left(C^\dagger\frac{\partial C}{\partial s}\right)_{\lambda'_1\lambda'_2}. \tag{A13}$$

We used that $\left(\frac{\partial D}{\partial s}\right)_{\lambda'_1\lambda'_2} = 0$ if $\lambda'_1 \neq \lambda'_2$ because D is taken to be diagonal. Substituting $s = \Omega_{k\lambda_1\lambda_2}$, we get

$$\frac{\partial C_{k\lambda\lambda'}}{\partial\Omega_{k\lambda_1\lambda_2}} = \sum_{\lambda'_1} C_{k\lambda\lambda'_1}\frac{C^*_{k\lambda_1\lambda'_1}C_{k\lambda_2\lambda'}}{\Omega_{k\lambda'} - \Omega_{k\lambda'_1}}. \tag{A14}$$

In the same way, we get

$$\frac{\partial C^*_{k\lambda\lambda'}}{\partial\Omega_{k\lambda_1\lambda_2}} = \sum_{\lambda'_1} \frac{C^*_{k\lambda_1\lambda'}C_{k\lambda_2\lambda'_1}}{\Omega_{k\lambda'} - \Omega_{k\lambda'_1}}C^*_{k\lambda\lambda'_1}. \tag{A15}$$

The sums in Eqs. (A14) and (A15) are taken over the modes that are not degenerate to $\Omega_{k\lambda'}$ because the contribution from the degenerate modes can be made vanish by using the degrees of freedom in unitary transformation.

Using the formulas above, the gradient of the variational free energy with respect to the SCP dynamical matrix is derived as

$$\frac{\partial\mathcal{F}}{\partial\Omega_{k\lambda_1\lambda_2}} = \sum_{\lambda'} \left[\frac{\hbar}{2}\frac{\partial}{\partial\Omega_{k\lambda'}}\left(\frac{n_B + 1/2}{\Omega_{k\lambda'}}\right)C^*_{k\lambda_1\lambda'}C_{k\lambda_2\lambda'}\right.$$

$$\times \left\{-\Omega^2_{k\lambda'} + \widetilde{\Phi}(-k\lambda', k\lambda')\right.$$

$$+ \sum_{n=2}^{\infty} \frac{1}{(n-1)!N^{n-1}} \sum_{\{k\lambda'\}} \left(\frac{\hbar}{2}\right)^{n-1}$$

$$\times \frac{\widetilde{\Phi}(-k\lambda', k\lambda', k_1\lambda'_1, -k_1\lambda'_1, \cdots, -k_{n-1}\lambda'_{n-1})}{\Omega_{k_1\lambda'_1}\cdots\Omega_{k_{n-1}\lambda'_{n-1}}}$$

$$\left.\left.\left(n_B(\hbar\Omega_{k_1\lambda'_1}) + \frac{1}{2}\right)\cdots\left(n_B(\hbar\Omega_{k_{n-1}\lambda'_{n-1}}) + \frac{1}{2}\right)\right\}\right] \tag{A16}$$

$$+ \sum_{\lambda'\lambda'_1} \left[\frac{\hbar}{2}\frac{n_B(\hbar\Omega_{k\lambda'}) + 1/2}{\Omega_{k\lambda'}}\frac{C^*_{k\lambda_1\lambda'}C_{k\lambda_2\lambda'_1}}{\Omega_{k\lambda'} - \Omega_{k\lambda'_1}}\right.$$

$$\times \left\{\sum_{n=1}^{\infty} \frac{1}{(n-1)!N^{n-1}} \sum_{\{k\lambda'\}} \left(\frac{\hbar}{2}\right)^{n-1}\right.$$

$$\times \frac{\widetilde{\Phi}(-k\lambda'_1, k\lambda', k_2\lambda'_2, -k_2\lambda'_2, \cdots, -k_{n-1}\lambda'_{n-1})}{\Omega_{k_2\lambda'_2}\cdots\Omega_{k_n\lambda'_n}}$$

$$\left.\left.\times \left(n_B(\hbar\Omega_{k_2\lambda'_2}) + \frac{1}{2}\right)\cdots\left(n_B(\hbar\Omega_{k_n\lambda'_n}) + \frac{1}{2}\right)\right\}\right] \tag{A17}$$

$$+ \frac{\hbar}{2}\frac{n_B(\hbar\Omega_{k\lambda'}) + 1/2}{\Omega_{k\lambda'}}\frac{C^*_{k\lambda_1\lambda'_1}C_{k\lambda_2\lambda'}}{\Omega_{k\lambda'} - \Omega_{k\lambda'_1}}$$

$$\times \left\{\sum_{n=1}^{\infty} \frac{1}{(n-1)!N^{n-1}} \sum_{\{k\lambda'\}} \left(\frac{\hbar}{2}\right)^{n-1}\right.$$

$$\times \frac{\widetilde{\Phi}(-k\lambda', k\lambda'_1, k_2\lambda'_2, -k_2\lambda'_2, \cdots, -k_n\lambda'_n)}{\Omega_{k_2\lambda'_2}\cdots\Omega_{k_n\lambda'_n}}$$

$$\left.\left.\times \left(n_B(\hbar\Omega_{k_2\lambda'_2}) + \frac{1}{2}\right)\cdots\left(n_B(\hbar\Omega_{k_n\lambda'_n}) + \frac{1}{2}\right)\right\}\right]. \tag{A18}$$

The variational condition is that the terms in the curly brackets in Eqs. (A16)~(A18) all vanish. In the original-mode representation, these three conditions can be put together to a single

SCP equation

$$\Omega^2_{\boldsymbol{k}\lambda_1\lambda_2}$$
$$= \sum_{n=1}^{\infty} \frac{1}{(n-1)!N^{n-1}} \sum_{\{\boldsymbol{k}\lambda'\}} \left(\frac{\hbar}{2}\right)^{n-1}$$
$$\frac{\widetilde{\Phi}(-\boldsymbol{k}\lambda_1, \boldsymbol{k}\lambda_2, \boldsymbol{k}_1\lambda'_1, -\boldsymbol{k}_1\lambda'_1, \cdots, -\boldsymbol{k}_{n-1}\lambda'_{n-1})}{\Omega_{\boldsymbol{k}_1\lambda'_1} \cdots \Omega_{\boldsymbol{k}_{n-1}\lambda'_{n-1}}}$$
$$\times \left(n_B(\hbar\Omega_{\boldsymbol{k}_1\lambda'_1}) + \frac{1}{2}\right) \cdots \left(n_B(\hbar\Omega_{\boldsymbol{k}_{n-1}\lambda'_{n-1}}) + \frac{1}{2}\right) \qquad \text{(A19)}$$

Appendix B: Calculation of the Hessian of the SCP free energy

The Hessian of the SCP free energy is useful in discussing the stability of the crystal structure at given conditions. In this Appendix, we discuss the formulation to calculate the Hessian, whose implementation is a future task. We derive the Hessian with respect to the internal coordinates. The Hessian for the strain and the mixed derivatives can be calculated in the same manner. We start from the general formula for the derivative

$$\frac{\partial^2 \mathcal{F}(\widetilde{\Phi}^{(q^{(0)}, u_{\mu\nu})}, \Omega_{\boldsymbol{k}\lambda_1\lambda_2}(q^{(0)}_\lambda, u_{\mu\nu}))}{\partial q^{(0)}_{\lambda_1} \partial q^{(0)}_{\lambda_2}}$$
$$= \left(\frac{\partial}{\partial q^{(0)}_{\lambda_1}} + \sum_{\boldsymbol{k}\lambda_3\lambda_4} \frac{\partial \Omega_{\boldsymbol{k}\lambda_3\lambda_4}}{\partial q^{(0)}_{\lambda_1}} \frac{\partial}{\partial \Omega_{\boldsymbol{k}\lambda_3\lambda_4}}\right)$$
$$\times \left(\frac{\partial}{\partial q^{(0)}_{\lambda_2}} + \sum_{\boldsymbol{k}\lambda_3\lambda_4} \frac{\partial \Omega_{\boldsymbol{k}\lambda_3\lambda_4}}{\partial q^{(0)}_{\lambda_2}} \frac{\partial}{\partial \Omega_{\boldsymbol{k}\lambda_3\lambda_4}}\right) \mathcal{F}(q^{(0)}_\lambda, u_{\mu\nu}, \Omega_{\boldsymbol{k}\lambda_1\lambda_2}),$$
$$\text{(B1)}$$

where $\Omega_{\boldsymbol{k}\lambda_1\lambda_2}(q^{(0)}_\lambda, u_{\mu\nu})$ is the solution of the SCP equation in the crystal structure given by $q^{(0)}_\lambda$, $u_{\mu\nu}$. Since the solution of the SCP equation satisfies the variational condition, we can simplify the RHS by using

$$\left(\frac{\partial}{\partial q^{(0)}_\lambda} + \sum_{\boldsymbol{k}\lambda_1\lambda_2} \frac{\partial \Omega_{\boldsymbol{k}\lambda_1\lambda_2}}{\partial q^{(0)}_\lambda} \frac{\partial}{\partial \Omega_{\boldsymbol{k}\lambda_1\lambda_2}}\right) \frac{\partial \mathcal{F}}{\partial \Omega_{\boldsymbol{k}\lambda_3\lambda_4}} = 0, \qquad \text{(B2)}$$

as

$$\frac{\partial^2 \mathcal{F}(\widetilde{\Phi}^{(q^{(0)}, u_{\mu\nu})}, \Omega(q^{(0)}_\lambda, u_{\mu\nu}))}{\partial q^{(0)}_{\lambda_1} \partial q^{(0)}_{\lambda_2}}$$
$$= \frac{\partial^2 \mathcal{F}(\widetilde{\Phi}^{(q^{(0)}, u_{\mu\nu})}, \Omega)}{\partial q^{(0)}_{\lambda_1} \partial q^{(0)}_{\lambda_2}} + \sum_{\boldsymbol{k}\lambda_3\lambda_4} \frac{\partial \Omega_{\boldsymbol{k}\lambda_3\lambda_4}}{\partial q^{(0)}_{\lambda_1}} \frac{\partial^2 \mathcal{F}}{\partial q^{(0)}_{\lambda_2} \partial \Omega_{\boldsymbol{k}\lambda_3\lambda_4}}.$$
$$\text{(B3)}$$

Let us estimate each term in the RHS of Eq. (B3). The first term is rewritten by the SCP dynamical matrix

$$\frac{\partial^2 \mathcal{F}(\widetilde{\Phi}^{(q^{(0)}, u_{\mu\nu})}, \Omega)}{\partial q^{(0)}_{\lambda_1} \partial q^{(0)}_{\lambda_2}}$$
$$= N \times \sum_{n=0}^{\infty} \frac{1}{n!N^n} \sum_{\{\boldsymbol{k}\lambda'\}} \left(\frac{\hbar}{2}\right)^n$$
$$\times \frac{\widetilde{\Phi}(\boldsymbol{k}_1\lambda'_1, -\boldsymbol{k}_1\lambda'_1, \cdots, \boldsymbol{k}_n\lambda'_n, -\boldsymbol{k}_n\lambda'_n, \boldsymbol{0}\lambda_1, \boldsymbol{0}\lambda_2)}{\Omega_{\boldsymbol{k}_1\lambda'_1} \cdots \Omega_{\boldsymbol{k}_1\lambda'_1}}$$
$$\times \left(n_B(\hbar\Omega_{\boldsymbol{k}_1\lambda'_1}) + \frac{1}{2}\right) \cdots \left(n_B(\hbar\Omega_{\boldsymbol{k}_n\lambda'_n}) + \frac{1}{2}\right)$$
$$= N\Omega^2_{\boldsymbol{0}\lambda_1\lambda_2}. \qquad \text{(B4)}$$

The second term is more complicated. $\frac{\partial^2 \mathcal{F}}{\partial q^{(0)}_{\lambda_2} \partial \Omega_{\boldsymbol{k}\lambda_3\lambda_4}}$ is expanded as

$$\frac{\partial^2 \mathcal{F}}{\partial q^{(0)}_\lambda \partial \Omega_{\boldsymbol{k}\lambda_1\lambda_2}}$$
$$= N \times \sum_{n=1}^{\infty} \frac{1}{(n-1)!N^n} \sum_{\{\boldsymbol{k}\lambda'\}} \left(\frac{\hbar}{2}\right)^n$$
$$\times \frac{\widetilde{\Phi}(\boldsymbol{k}\lambda'_1, -\boldsymbol{k}\lambda'_1, \boldsymbol{k}_2\lambda'_2, -\boldsymbol{k}_2\lambda'_2, \cdots, \boldsymbol{k}_n\lambda'_n, -\boldsymbol{k}_n\lambda'_n, \boldsymbol{0}\lambda)}{\Omega_{\boldsymbol{k}_2\lambda'_2} \cdots \Omega_{\boldsymbol{k}_n\lambda'_n}}$$
$$\times \left(n_B(\hbar\Omega_{\boldsymbol{k}_2\lambda'_2}) + \frac{1}{2}\right) \cdots \left(n_B(\hbar\Omega_{\boldsymbol{k}_n\lambda'_n}) + \frac{1}{2}\right)$$
$$\times \frac{\partial \Omega_{\boldsymbol{k}\lambda'_1}}{\partial \Omega_{\boldsymbol{k}\lambda_1\lambda_2}} \frac{\partial}{\partial \Omega_{\boldsymbol{k}\lambda'_1}} \left(n_B(\hbar\Omega_{\boldsymbol{k}\lambda'_1}) + \frac{1}{2}\right)$$
$$+ N \times \sum_{n=1}^{\infty} \frac{1}{(n-1)!N^n} \sum_{\{\boldsymbol{k}\lambda'\}} \left(\frac{\hbar}{2}\right)^n \sum_{\lambda_3\lambda_4}$$
$$\times \frac{\widetilde{\Phi}(\boldsymbol{k}\lambda_3, -\boldsymbol{k}\lambda_4, \boldsymbol{k}_2\lambda'_2, -\boldsymbol{k}_2\lambda'_2, \cdots, \boldsymbol{k}_n\lambda'_n, -\boldsymbol{k}_n\lambda'_n, \boldsymbol{0}\lambda)}{\Omega_{\boldsymbol{k}_1\lambda'_1} \cdots \Omega_{\boldsymbol{k}_n\lambda'_n}}$$
$$\times \left(n_B(\hbar\Omega_{\boldsymbol{k}\lambda'_1}) + \frac{1}{2}\right) \cdots \left(n_B(\hbar\Omega_{\boldsymbol{k}_n\lambda'_n}) + \frac{1}{2}\right)$$
$$\times \frac{\partial}{\partial \Omega_{\boldsymbol{k}\lambda_1\lambda_2}} (C_{\boldsymbol{k}\lambda_3\lambda'_1} C^*_{\boldsymbol{k}\lambda_4\lambda'_1}). \qquad \text{(B5)}$$

The derivative $\frac{\partial \Omega_{\boldsymbol{k}\lambda_3\lambda_4}}{\partial q^{(0)}_{\lambda_1}}$ cannot be analytically calculated. Thus, we derive a self-consistent equation of $\frac{\partial \Omega_{\boldsymbol{k}\lambda_3\lambda_4}}{\partial q^{(0)}_{\lambda_1}}$ by differentiat-

ing the both sides of the SCP equation.

$$
\begin{aligned}
&\frac{\partial \Omega^2_{\boldsymbol{k}\lambda_1\lambda_2}}{\partial q^{(0)}_\lambda} \\
&= \sum_{n=0}^\infty \frac{1}{n!N^n} \sum_{\{\boldsymbol{k}\lambda'\}} \left(\frac{\hbar}{2}\right)^n \\
&\times \frac{\widetilde{\Phi}(-\boldsymbol{k}\lambda_1, -\boldsymbol{k}\lambda_2, \boldsymbol{k}_1\lambda'_1, -\boldsymbol{k}_1\lambda'_1, \cdots, \boldsymbol{k}_n\lambda'_n, -\boldsymbol{k}_n\lambda'_n, \boldsymbol{0}\lambda)}{\Omega_{\boldsymbol{k}_1\lambda'_1} \cdots \Omega_{\boldsymbol{k}_n\lambda'_n}} \\
&\times \left(n_B(\hbar\Omega_{\boldsymbol{k}_1\lambda'_1}) + \frac{1}{2}\right) \cdots \left(n_B(\hbar\Omega_{\boldsymbol{k}_n\lambda'_n}) + \frac{1}{2}\right) \\
&+ \sum_{n=1}^\infty \frac{1}{(n-1)!N^n} \sum_{\{\boldsymbol{k}\lambda'\}} \left(\frac{\hbar}{2}\right)^n \\
&\times \frac{\widetilde{\Phi}(-\boldsymbol{k}\lambda_1, -\boldsymbol{k}\lambda_2, \boldsymbol{k}_1\lambda'_1, -\boldsymbol{k}_1\lambda'_1, \cdots, \boldsymbol{k}_n\lambda'_n, -\boldsymbol{k}_n\lambda'_n, \boldsymbol{0}\lambda)}{\Omega_{\boldsymbol{k}_2\lambda'_2} \cdots \Omega_{\boldsymbol{k}_n\lambda'_n}} \\
&\times \left(n_B(\hbar\Omega_{\boldsymbol{k}_2\lambda'_2}) + \frac{1}{2}\right) \cdots \left(n_B(\hbar\Omega_{\boldsymbol{k}_n\lambda'_n}) + \frac{1}{2}\right) \\
&\times \sum_{\lambda_3\lambda_4} \frac{\partial \Omega_{\boldsymbol{k}_1\lambda_3\lambda_4}}{\partial q^{(0)}_\lambda} \frac{\partial \Omega_{\boldsymbol{k}_1\lambda'_1}}{\partial \Omega_{\boldsymbol{k}_1\lambda_3\lambda_4}} \frac{\partial}{\partial \Omega_{\boldsymbol{k}_1\lambda'_1}} \left(\frac{n_B(\Omega_{\boldsymbol{k}_1\lambda'_1}) + 1/2}{\Omega_{\boldsymbol{k}_1\lambda'_1}}\right) \\
&+ \sum_{n=1}^\infty \frac{1}{(n-1)!N^n} \sum_{\{\boldsymbol{k}\lambda'\}} \left(\frac{\hbar}{2}\right)^n \sum_{\lambda_3\lambda_4} \\
&\times \frac{\widetilde{\Phi}(-\boldsymbol{k}\lambda_1, -\boldsymbol{k}\lambda_2, \boldsymbol{k}_1\lambda_3, -\boldsymbol{k}_1\lambda_4, \cdots, \boldsymbol{k}_n\lambda'_n, -\boldsymbol{k}_n\lambda'_n, \boldsymbol{0}\lambda)}{\Omega_{\boldsymbol{k}_1\lambda'_1} \cdots \Omega_{\boldsymbol{k}_n\lambda'_n}} \\
&\times \left(n_B(\hbar\Omega_{\boldsymbol{k}_1\lambda'_1}) + \frac{1}{2}\right) \cdots \left(n_B(\hbar\Omega_{\boldsymbol{k}_n\lambda'_n}) + \frac{1}{2}\right) \\
&\times \sum_{\lambda_5\lambda_6} \frac{\partial \Omega_{\boldsymbol{k}_1\lambda_5\lambda_6}}{\partial q^{(0)}_\lambda} \frac{\partial}{\partial \Omega_{\boldsymbol{k}_1\lambda_5\lambda_6}} (C_{\boldsymbol{k}_1\lambda_3\lambda'_1} C^*_{\boldsymbol{k}_1\lambda_4\lambda'_1})
\end{aligned} \tag{B6}
$$

We get $\frac{\partial \Omega^2_{\boldsymbol{k}\lambda_1\lambda_2}}{\partial q^{(0)}_\lambda}$ or $\frac{\partial \Omega_{\boldsymbol{k}\lambda_1\lambda_2}}{\partial q^{(0)}_\lambda}$ by solving Eq. (B6) self-consistently. Substituting the solution to Eq. (B5) and then to Eq. (B3), it is possible to calculate the Hessian of the SCP free energy and discuss the stability of crystal structures at finite temperature.

Appendix C: Implementation details of the IFC renormalization.

In this Appendix, we explain the details of the implementation of the IFC renormalization to the ALAMODE package. We truncate the Taylor expansion of the potential energy surface at the fourth-order, which is the approximation in the ALAMODE implementation of the SCP calculation.

The IFC renormalization by strain is written down in real-space representation as shown in Eq. (15). However, the Fourier transformation of the anharmonic IFCs is so computationally costly that it is not feasible to Fourier-transform the anharmonic IFCs at every step of the structural optimization. Therefore, the derivatives of the IFCs with respect to the strain and their Fourier transformation are calculated in the pre-calculation before the structural optimization process. For the first-order IFCs, the following quantities are calculated.

$$
\frac{\partial \widetilde{\Phi}(\boldsymbol{0}\lambda_1)}{\partial u_{\mu\nu}}\bigg|_{q^{(0)}=0, u_{\mu\nu}=0} = \sum_{\alpha_1\mu_1} \frac{\epsilon_{\boldsymbol{0}\lambda_1, \alpha_1\mu_1}}{\sqrt{M_{\alpha_1}}} \sum_{\boldsymbol{R}'_1\alpha'_1} \Phi^{(0)}_{\mu_1\mu}(\boldsymbol{0}\alpha_1, \boldsymbol{R}'_1\alpha'_1) R'_{1\alpha'_1\nu} \tag{C1}
$$

$$
\frac{\partial^2 \widetilde{\Phi}(\boldsymbol{0}\lambda_1)}{\partial u_{\mu_1\nu_1} \partial u_{\mu_2\nu_2}}\bigg|_{q^{(0)}=0, u_{\mu\nu}=0} = \sum_{\alpha_1\mu'_1} \frac{\epsilon_{\boldsymbol{0}\lambda_1, \alpha_1\mu'_1}}{\sqrt{M_{\alpha_1}}} \sum_{\{\boldsymbol{R}'\alpha'\}} \Phi^{(0)}_{\mu'_1\mu_1\mu_2}(\boldsymbol{0}\alpha_1, \boldsymbol{R}'_1\alpha'_1, \boldsymbol{R}'_2\alpha'_2) R'_{1\alpha'_1\nu_1} R'_{2\alpha'_2\nu_2} \tag{C2}
$$

$$
\frac{\partial^3 \widetilde{\Phi}(\boldsymbol{0}\lambda_1)}{\partial u_{\mu_1\nu_1} \partial u_{\mu_2\nu_2} \partial u_{\mu_3\nu_3}}\bigg|_{q^{(0)}=0, u_{\mu\nu}=0} = \sum_{\alpha_1\mu'_1} \frac{\epsilon_{\boldsymbol{0}\lambda_1, \alpha_1\mu'_1}}{\sqrt{M_{\alpha_1}}} \sum_{\{\boldsymbol{R}'\alpha'\}} \Phi^{(0)}_{\mu'_1\mu_1\mu_2\mu_3}(\boldsymbol{0}\alpha_1, \boldsymbol{R}'_1\alpha'_1, \boldsymbol{R}'_2\alpha'_2, \boldsymbol{R}'_3\alpha'_3) R'_{1\alpha'_1\nu_1} R'_{2\alpha'_2\nu_2} R'_{3\alpha'_3\nu_3} \tag{C3}
$$

$\Phi^{(0)} = \Phi^{(q^{(0)}=0, u_{\mu\nu}=0)}$ is the IFC in the reference structure

without atomic displacements nor cell deformation. For the harmonic and cubic IFCs, we calculate

$$\left.\frac{\partial \widetilde{\Phi}(\boldsymbol{k}_1\lambda_1, -\boldsymbol{k}_1\lambda_2)}{\partial u_{\mu_1\nu_1}}\right|_{q^{(0)}=0, u_{\mu\nu}=0} = \sum_{\{\alpha\mu'\}} \frac{\epsilon_{\boldsymbol{k}_1\lambda_1, \alpha_1\mu_1'}}{\sqrt{M_{\alpha_1}}} \frac{\epsilon_{-\boldsymbol{k}_1\lambda_2, \alpha_2\mu_2'}}{\sqrt{M_{\alpha_2}}} \sum_{\boldsymbol{R}_1} e^{i\boldsymbol{k}_1\cdot\boldsymbol{R}_1}$$
$$\times \sum_{\boldsymbol{R}_1'\alpha_1'} \Phi^{(0)}_{\mu_1'\mu_2'\mu_1}(\boldsymbol{R}_1\alpha_1, \boldsymbol{0}\alpha_2, \boldsymbol{R}_1'\alpha_1') R'_{1\alpha_1'\nu_1} \tag{C4}$$

$$\left.\frac{\partial^2 \widetilde{\Phi}(\boldsymbol{k}_1\lambda_1, -\boldsymbol{k}_1\lambda_2)}{\partial u_{\mu_1\nu_1}\partial u_{\mu_2\nu_2}}\right|_{q^{(0)}=0, u_{\mu\nu}=0} = \sum_{\{\alpha\mu'\}} \frac{\epsilon_{\boldsymbol{k}_1\lambda_1, \alpha_1\mu_1'}}{\sqrt{M_{\alpha_1}}} \frac{\epsilon_{-\boldsymbol{k}_1\lambda_2, \alpha_2\mu_2'}}{\sqrt{M_{\alpha_2}}} \sum_{\boldsymbol{R}_1} e^{i\boldsymbol{k}_1\cdot\boldsymbol{R}_1}$$
$$\times \sum_{\{\boldsymbol{R}'\alpha'\}} \Phi^{(0)}_{\mu_1'\mu_2'\mu_1\mu_2}(\boldsymbol{R}_1\alpha_1, \boldsymbol{0}\alpha_2, \boldsymbol{R}_1'\alpha_1', \boldsymbol{R}_2'\alpha_2') R'_{1\alpha_1'\nu_1} R'_{2\alpha_2'\nu_2} \tag{C5}$$

$$\left.\frac{\partial \widetilde{\Phi}(\boldsymbol{0}\lambda_1, \boldsymbol{k}_1\lambda_2, -\boldsymbol{k}_1\lambda_3)}{\partial u_{\mu_1\nu_1}}\right|_{q^{(0)}=0, u_{\mu\nu}=0} = \sum_{\{\alpha\mu'\}} \frac{\epsilon_{\boldsymbol{0}\lambda_1, \alpha_1\mu_1'}}{\sqrt{M_{\alpha_1}}} \frac{\epsilon_{\boldsymbol{k}_1\lambda_2, \alpha_2\mu_2'}}{\sqrt{M_{\alpha_2}}} \frac{\epsilon_{-\boldsymbol{k}_1\lambda_3, \alpha_3\mu_3'}}{\sqrt{M_{\alpha_3}}} \sum_{\boldsymbol{R}_1\boldsymbol{R}_2} e^{i\boldsymbol{k}_1\cdot\boldsymbol{R}_2}$$
$$\times \sum_{\boldsymbol{R}_1'\alpha_1'} \Phi^{(0)}_{\mu_1'\mu_2'\mu_3'\mu_1}(\boldsymbol{R}_1\alpha_1, \boldsymbol{R}_2\alpha_2, \boldsymbol{0}\alpha_3, \boldsymbol{R}_1'\alpha_1') R'_{1\alpha_1'\nu_1} \tag{C6}$$

For the cubic IFCs, it is enough to calculate the derivatives of the IFCs of the form $\widetilde{\Phi}(\boldsymbol{0}\lambda_1, \boldsymbol{k}\lambda_2, -\boldsymbol{k}\lambda_3)$. The quartic IFCs are not changed because the higher-order IFCs are truncated in the Taylor expansion. It should be noted that the fractional coordinates of the k-points in the Brillouin zone are kept fixed in these derivatives. This makes the k-mesh adapt to the deformed Brillouin zone, which is convenient for calculating the free energy per unit cell. In addition, this convention simplifies the formulas of the IFC renormalization because it keeps the $\boldsymbol{k}\cdot\boldsymbol{R}$ terms invariant when the lattice vectors are changed.

Special care needs to be taken for the zeroth-order IFC (constant term of the potential energy surface) because the surface effect must be properly considered to derive similar formulas [60], which is quite complicated. Therefore, we directly calculate the second-order and third-order elastic constants by fitting the strain-energy relation. Although the elastic constants are usually defined as quantities per unit volume, we

define them as the quantities per unit cell as

$$C_{\mu_1\nu_1, \mu_2\nu_2} = \frac{1}{N} \frac{\partial^2 U_0}{\partial \eta_{\mu_1\nu_1}\partial \eta_{\mu_2\nu_2}}, \tag{C7}$$

$$C_{\mu_1\nu_1, \mu_2\nu_2, \mu_3\nu_3} = \frac{1}{N} \frac{\partial^2 U_0}{\partial \eta_{\mu_1\nu_1}\partial \eta_{\mu_2\nu_2}\partial \eta_{\mu_3\nu_3}}, \tag{C8}$$

for later convenience. The strain tensor $\eta_{\mu\nu}$ is defined as

$$\eta_{\mu\nu} = \frac{1}{2}\left(\sum_{\mu'}(\delta_{\mu\mu'}+u_{\mu\mu'})(\delta_{\nu\mu'}+u_{\nu\mu'}) - \delta_{\mu\nu}\right) \tag{C9}$$

$$= \frac{1}{2}\left(u_{\mu\nu}+u_{\nu\mu}+\sum_{\mu'}u_{\mu\mu'}u_{\nu\mu'}\right). \tag{C10}$$

There is one-to-one correspondence between $u_{\mu\nu}$ and $\eta_{\mu\nu}$ as long as we restict $u_{\mu\nu}$ to be symmetric. The number of strain modes to calculate can be decreased using the crystal symmetry [63, 64]. Note that although the internal coordinates are relaxed in calculations to reproduce experimentally observed elastic constants [63, 64], we run the DFT calculations with fixed internal coordinates because the internal coordinates are treated separately as independent degrees of freedom.

Therefore, the IFCs in the reciprocal space representation for the strained cell can be calculated by

$$\frac{1}{N}U_0^{(q^{(0)}=0, u_{\mu\nu})} = \frac{1}{2}\sum_{\mu_1\nu_1, \mu_2\nu_2} C_{\mu_1\nu_1, \mu_2\nu_2}\eta_{\mu_1\nu_1}\eta_{\mu_2\nu_2} + \frac{1}{6}\sum_{\mu_1\nu_1, \mu_2\nu_2, \mu_3\nu_3} C_{\mu_1\nu_1, \mu_2\nu_2, \mu_3\nu_3}\eta_{\mu_1\nu_1}\eta_{\mu_2\nu_2}\eta_{\mu_3\nu_3}, \tag{C11}$$

$$\widetilde{\Phi}^{(q^{(0)}=0,u_{\mu\nu})}(\mathbf{0}\lambda) = \widetilde{\Phi}^{(q^{(0)}=0,u_{\mu\nu}=0)}(\mathbf{0}\lambda) + \sum_{\mu_1\nu_1} \frac{\partial\widetilde{\Phi}(\mathbf{0}\lambda_1)}{\partial u_{\mu_1\nu_1}} u_{\mu_1\nu_1}$$
$$+ \frac{1}{2}\sum_{\{\mu_1\nu\}} \frac{\partial^2\widetilde{\Phi}(\mathbf{0}\lambda_1)}{\partial u_{\mu_1\nu_1}\partial u_{\mu_2\nu_2}} u_{\mu_1\nu_1} u_{\mu_2\nu_2} + \frac{1}{6}\sum_{\{\mu_1\nu\}} \frac{\partial^3\widetilde{\Phi}(\mathbf{0}\lambda_1)}{\partial u_{\mu_1\nu_1}\partial u_{\mu_2\nu_2}\partial u_{\mu_3\nu_3}} u_{\mu_1\nu_1} u_{\mu_2\nu_2} u_{\mu_3\nu_3}, \tag{C12}$$

$$\widetilde{\Phi}^{(q^{(0)}=0,u_{\mu\nu})}(\mathbf{k}_1\lambda_1, -\mathbf{k}_1\lambda_2) = \widetilde{\Phi}^{(q^{(0)}=0,u_{\mu\nu}=0)}(\mathbf{k}_1\lambda_1, -\mathbf{k}_1\lambda_2) + \sum_{\mu_1\nu_1} \frac{\partial\widetilde{\Phi}(\mathbf{k}_1\lambda_1, -\mathbf{k}_1\lambda_2)}{\partial u_{\mu_1\nu_1}} u_{\mu_1\nu_1}$$
$$+ \frac{1}{2}\sum_{\{\mu\nu\}} \frac{\partial\widetilde{\Phi}(\mathbf{k}_1\lambda_1, -\mathbf{k}_1\lambda_2)}{\partial u_{\mu_1\nu_1}\partial u_{\mu_2\nu_2}} u_{\mu_1\nu_1} u_{\mu_2\nu_2}, \tag{C13}$$

$$\widetilde{\Phi}^{(q^{(0)}=0,u_{\mu\nu})}(\mathbf{0}\lambda_1, \mathbf{k}_1\lambda_2, -\mathbf{k}_1\lambda_3) = \widetilde{\Phi}^{(q^{(0)}=0,u_{\mu\nu}=0)}(\mathbf{0}\lambda_1, \mathbf{k}_1\lambda_2, -\mathbf{k}_1\lambda_3) + \sum_{\mu_1\nu_1} \frac{\partial\widetilde{\Phi}(\mathbf{0}\lambda_1, \mathbf{k}_1\lambda_2, -\mathbf{k}_1\lambda_3)}{\partial u_{\mu_1\nu_1}} u_{\mu_1\nu_1}, \tag{C14}$$

$$\widetilde{\Phi}^{(q^{(0)}=0,u_{\mu\nu})}(\mathbf{k}_1\lambda_1, -\mathbf{k}_1\lambda_2, \mathbf{k}_2\lambda_3, -\mathbf{k}_2\lambda_4) = \widetilde{\Phi}^{(q^{(0)}=0,u_{\mu\nu}=0)}(\mathbf{k}_1\lambda_1, -\mathbf{k}_1\lambda_2, \mathbf{k}_2\lambda_3, -\mathbf{k}_2\lambda_4). \tag{C15}$$

The first-order term is not included in Eq. (C11) because the stress tensor is assumed to vanish in the reference structure, which assumption can be relaxed straightforwardly. We also set $U_0^{(q^{(0)}=0,u_{\mu\nu}=0)} = 0$ without loss of generality. Substituting the $\widetilde{\Phi}^{(q^{(0)}=0,u_{\mu\nu})}$ obtained in the above formulas to the RHS of Eq. (11), we get the IFCs in arbitrary structures $\widetilde{\Phi}^{(q^{(0)},u_{\mu\nu})}$.

Similarly, the derivatives of the even-order IFCs with respect to the structural degrees of freedom are calculated as

$$\frac{1}{N}\frac{\partial U_0^{(q^{(0)},u_{\mu\nu})}}{\partial u_{\mu\nu}} = \sum_{\mu'\nu'} \frac{\partial\eta_{\mu'\nu'}}{\partial u_{\mu\nu}}\left(\sum_{\mu_1\nu_1} C_{\mu_1\nu_1,\mu'\nu'}\eta_{\mu_1\nu_1} + \frac{1}{3}\sum_{\mu_1\nu_1,\mu_2\nu_2} C_{\mu_1\nu_1,\mu_2\nu_2,\mu'\nu'}\eta_{\mu_1\nu_1}\eta_{\mu_2\nu_2}\right)$$
$$+ \sum_{m=1}^{3} \frac{1}{m!}\sum_{\{\lambda\}} \frac{\partial\widetilde{\Phi}^{(q^{(0)}=0,u_{\mu\nu})}(\mathbf{0}\lambda_1, \cdots, \mathbf{0}\lambda_m)}{\partial u_{\mu\nu}} q_{\lambda_1}^{(0)}\cdots q_{\lambda_m}^{(0)}, \tag{C16}$$

$$\frac{\partial\widetilde{\Phi}^{(q^{(0)},u_{\mu\nu})}(\mathbf{k}_1\lambda_1, -\mathbf{k}_1\lambda_2)}{\partial u_{\mu\nu}} = \frac{\partial\widetilde{\Phi}(\mathbf{k}_1\lambda_1, -\mathbf{k}_1\lambda_2)}{\partial u_{\mu\nu}} + \sum_{\mu'\nu'} \frac{\partial^2\widetilde{\Phi}(\mathbf{k}_1\lambda_1, -\mathbf{k}_1\lambda_2)}{\partial u_{\mu\nu}\partial u_{\mu'\nu'}} u_{\mu'\nu'}$$
$$+ \sum_{\rho_1} \frac{\partial\widetilde{\Phi}(\mathbf{k}_1\lambda_1, -\mathbf{k}_1\lambda_2, \mathbf{0}\rho_1)}{\partial u_{\mu\nu}} q_{\rho_1}^{(0)}, \tag{C17}$$

which are used in the calculation of the gradient of the SCP free energy.

Appendix D: Sum rules, symmetries, and mirror image conventions in IFC calculations

The IFCs need to satisfy several constraints to obtain physically reasonable results in phonon calculations. The permutation symmetry

$$\Phi_{\cdots\mu_i\cdots\mu_j\cdots}(\cdots, \mathbf{R}_i\alpha_i, \cdots, \mathbf{R}_j\alpha_j, \cdots)$$
$$= \Phi_{\cdots\mu_j\cdots\mu_i\cdots}(\cdots, \mathbf{R}_j\alpha_j, \cdots, \mathbf{R}_i\alpha_i, \cdots), \tag{D1}$$

the acoustic sum rule (ASR)

$$\sum_{\mathbf{R}_n\alpha_n} \Phi_{\mu_1\cdots\mu_{n-1}\mu_n}(\mathbf{R}_1\alpha_1, \cdots, \mathbf{R}_{n-1}\alpha_{n-1}, \mathbf{R}_n\alpha_n) = 0, \tag{D2}$$

and the space group symmetry are considered as they are especially important. The permutation symmetry is essential for the Hermiticity of the dynamical matrix. The acoustic sum rule must be satisfied to make the potential energy invariant under rigid translation of the whole system.

In first-principles phonon calculations, the size of the supercell is usually taken to be comparable to the interaction range because using larger supercells drastically increases the computational cost. Thus, the IFCs in the finite supercell and those in the infinite real space needs to be carefully distinguished in implementing a phonon calculation code. This distinction also plays an important role in considering the constraints on IFCs because they should be imposed in infinite real space, not in the finite supercell model, which have been frequently overlooked. In this research, we implement a program to the ALAMODE package [37, 55] to obtain IFCs that satisfy the permutation symmetry, ASR, and the space group symmetry in the infinite real space.

We begin with the definition and the relation of the IFCs in the supercell and those in the infinite real space. Consider that an atom in a two-dimensional 2×2 monatomic supercell (shaded area) is displaced, as shown in Fig. 11. In infinite real space, this situation corresponds to displacing all the mirror images of the atom, which are colored orange. Here, we
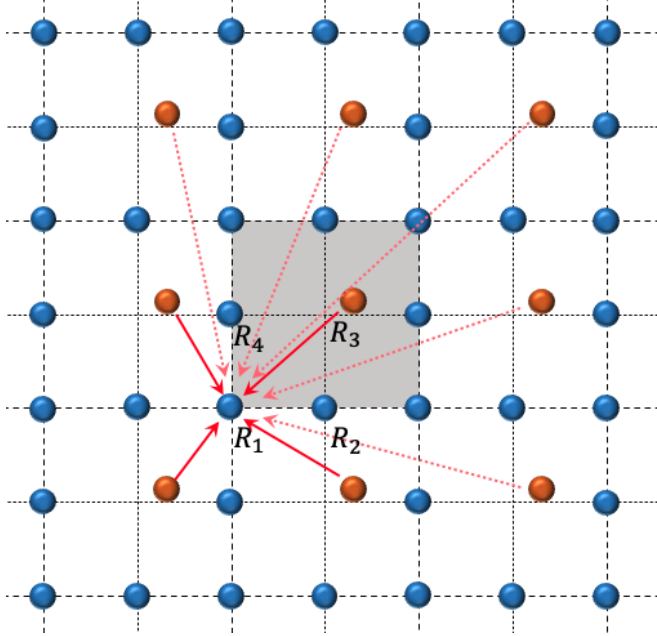

FIG. 11. Schematic figure of a two dimensional monatomic 2×2 supercell. The shaded part is the supercell considered in the calculation, which includes four primitive cells denoted $R_1, \cdots, R_4$. We consider that an atom in the supercell, which is colored orange, is displaced, which corresponds to displacing all the atoms in the real space which are colored orange.

temporarily assume that the potential is harmonic to discuss the relation between IFCs in the supercell and those in the infinite real space. The force that acts on the atom at R_1 in

Fig. 11 (lower-left corner in the supercell) is

$$f_{0\alpha\mu} = -\sum_{\nu} \Phi^{\text{supercell}}_{\mu\nu}(0\alpha, R_3\alpha)u_{R_3\alpha\nu}$$
$$= -\sum_{J}\sum_{\nu} \Phi_{\mu\nu}(0\alpha, R_3(J)\alpha)u_{R_3\alpha\nu}, \quad \text{(D3)}$$

where $\Phi^{\text{supercell}}$ are the IFCs in the supercell, and Φ are the IFCs in the infinite real space. In this appendix, we specify atoms in the infinite space by the combination $(R(J), \alpha)$. R is the position of the primitive cell in the considering supercell. The infinite space consists of periodically aligning supercells. J specifies the supercell which includes the considering atom. α is the atom number in the primitive cell. J for the first atom in IFCs is abbreviated because it can be fixed to the original supercell due to the translational invariance. From the above discussion, the relation between the harmonic IFCs in the real space and those in the supercell is

$$\Phi^{\text{supercell}}_{\mu_1\mu_2}(0\alpha_1, R\alpha_2) = \sum_{J} \Phi_{\mu_1\mu_2}(0\alpha_1, R(J)\alpha_2). \quad \text{(D4)}$$

The similar formula can be derived for the anharmonic IFCs.

$$\Phi^{\text{supercell}}_{\mu_1\cdots\mu_n}(0\alpha_1, R_2\alpha_2 \cdots R_n\alpha_n)$$
$$= \sum_{J_2\cdots J_n} \Phi_{\mu_1\mu_2\cdots\mu_n}(0\alpha_1, R_2(J_2)\alpha_2, \cdots, R_n(J_n)\alpha_n). \quad \text{(D5)}$$

These formulas show that the IFCs calculated in the supercell need to be distributed to the mirror images in infinite space. It is crucial to choose a proper convention when distributing IFCs because the reciprocal-space IFCs at incommensurate k-points are dependent on how to treat the mirror images. For the harmonic IFCs, equal values are usually assigned to the nearest mirror images, but the definition of nearest mirror images is not straightforward for anharmonic IFCs.

We then consider the physical constraints on the IFCs in the supercell and in the real space. We denote the distribution of IFCs to the mirror images as

$$\Phi_{\mu_1\cdots\mu_n}(0\alpha_1, \cdots R_n(J_n)\alpha_n)$$
$$= c^{J_2\cdots J_n}_{R_2\cdots R_n, \alpha_1\cdots\alpha_n, \mu_1\cdots\mu_n} \Phi^{\text{supercell}}_{\mu_1\cdots\mu_n}(0\alpha_1, \cdots R_n\alpha_n), \quad \text{(D6)}$$

where

$$\sum_{\{J\}} c^{J_2\cdots J_n}_{R_2\cdots R_n, \alpha_1\cdots\alpha_n, \mu_1\cdots\mu_n} = 1. \quad \text{(D7)}$$

We start with the discussion on the permutation symmetry. The permutation symmetry of the IFCs in the supercell is

$$\Phi^{\text{supercell}}_{\mu_1\cdots\mu_n}(0\alpha_1, \cdots R_n\alpha_n) = \Phi^{\text{supercell}}_{\mu'_1\cdots\mu'_n}(0\alpha'_1, \cdots R'_n\alpha'_n) \quad \text{(D8)}$$

where $(0\alpha'_1\mu'_1, \cdots R'_n\alpha'_n\mu'_n)$ is a combination of the atoms and the xyz components such that $(0\alpha_1\mu_1, \cdots R_n\alpha_n\mu_n)$ is permuted and translated to bring the first atom to the original primitive cell 0. On the other hand, the permutation symmetry of the IFCs in the real space is

$$\Phi_{\mu_1\cdots\mu_n}(0\alpha_1, \cdots R_n(J_n)\alpha_n) = \Phi_{\mu'_1\cdots\mu'_n}(0\alpha'_1, \cdots R'_n(J'_n)\alpha'_n), \quad \text{(D9)}$$

where $(\mathbf{0}\alpha_1'\mu_1', \cdots \mathbf{R}_n'(J_n')\alpha_n'\mu_n')$ is a combination of the atoms and xyz components such that $(\mathbf{0}\alpha_1\mu_1, \cdots \mathbf{R}_n(J_n)\alpha_n\mu_n)$ is permuted and translated to bring the first atom to the original primitive cell in the original supercell $\mathbf{R}(J) = \mathbf{0}(0)$. Thus, in addition to Eq. (D9), the c coefficients need to satisfy

$$c_{\mathbf{R}_2\cdots\mathbf{R}_n,\alpha_1\cdots\alpha_n,\mu_1\cdots\mu_n}^{J_2\cdots J_n} = c_{\mathbf{R}_2'\cdots\mathbf{R}_n',\alpha_1'\cdots\alpha_n',\mu_1'\cdots\mu_n'}^{J_2'\cdots J_n'} \tag{D10}$$

for the IFCs to satisfy permutation symmetry in the infinite space.

The acoustic sum rule in the supercell is

$$\sum_{\mathbf{R}_n\alpha_n} \Phi_{\mu_1\cdots\mu_{n-1}\mu_n}^{\text{supercell}}(\mathbf{0}\alpha_1, \cdots, \mathbf{R}_{n-1}\alpha_{n-1}, \mathbf{R}_n\alpha_n)$$
$$= \sum_{\mathbf{R}_n\alpha_n J_n} \left(\sum_{J_2\cdots J_{n-1}} \Phi_{\mu_1\cdots\mu_{n-1}\mu_n}(\mathbf{0}\alpha_1, \cdots, \mathbf{R}_{n-1}(J_{n-1})\alpha_{n-1}, \mathbf{R}_n(J_n)\alpha_n) \right)$$
$$= 0, \tag{D11}$$

for all $\mu_1, \cdots, \mu_n, \alpha_1, \cdots, \alpha_{n-1}, \mathbf{R}_2, \cdots, \mathbf{R}_{n-1}$, which is a weaker condition than ASR in the real space.

$$\sum_{\mathbf{R}_n J_n \alpha_n} \Phi_{\mu_1\cdots\mu_{n-1}\mu_n}(\mathbf{0}\alpha_1, \cdots, \mathbf{R}_{n-1}(J_{n-1})\alpha_{n-1}, \mathbf{R}_n(J_n)\alpha_n)$$
$$= \sum_{\mathbf{R}_n J_n \alpha_n} c_{\mathbf{R}_2\cdots\mathbf{R}_n,\alpha_1\cdots\alpha_n,\mu_1\cdots\mu_n}^{J_2\cdots J_n} \Phi_{\mu_1\cdots\mu_n}^{\text{supercell}}(\mathbf{0}\alpha_1, \cdots \mathbf{R}_n\alpha_n)$$
$$= 0, \tag{D12}$$

for all $\mu_1, \cdots, \mu_n, \alpha_1, \cdots, \alpha_{n-1}, \mathbf{R}_2(J_2), \cdots, \mathbf{R}_{n-1}(J_{n-1})$. In general, the coefficients $c_{\mathbf{R}_2\cdots\mathbf{R}_n,\alpha_1\cdots\alpha_n,\mu_1\cdots\mu_n}^{J_2\cdots J_n}$ need to be determined before calculating the IFCs in the supercell to impose the constraint of Eq. (D12). For the IFCs to satisfy the space group symmetry in the real space, the coefficients $c_{\mathbf{R}_2\cdots\mathbf{R}_n,\alpha_1\cdots\alpha_n,\mu_1\cdots\mu_n}^{J_2\cdots J_n}$ needs to be compatible with the symmetry operations, like the above discussion on the permutation symmetry.

Two conventions had been implemented in the ALAMODE package to distribute IFCs to the mirror images, which we discuss in relation with constraints on IFCs in the infinite real space. Both conventions distribute IFCs to the mirror images after calculating the IFCs in the supercell, which made it impossible to satisfy the permutation symmetry and the acoustic sum rule at the same time. In one convention, the IFCs are distributed to the mirror images that the sum of the distance between all pairs

$$\sum_{i \neq j} d_{\mathbf{R}_i(J_i)\alpha_i, \mathbf{R}_j(J_j)\alpha_j} \tag{D13}$$

is minimum. $d_{\mathbf{R}_i(J_i)\alpha_i, \mathbf{R}_j(J_j)\alpha_j}$ is the distance between the atoms $\mathbf{R}_i(J_i)\alpha_i$ and $\mathbf{R}_j(J_j)\alpha_j$. This way of determining $c_{\mathbf{R}_2\cdots\mathbf{R}_n,\alpha_1\cdots\alpha_n,\mu_1\cdots\mu_n}^{J_2\cdots J_n}$ is compatible with the permutation symmetry and the space group symmetry. The IFCs made in this convention satisfies the permutation symmetry and the space group symmetry in infinite space. However, ASR is broken in the infinite real space because Eq. (D12) is not imposed. In the other convention, the IFCs are distributed

to the mirror images in which the distances between the first atom and each of the other atoms ($d_{\mathbf{0}(0)\alpha_1, \mathbf{R}_i(J_i)\alpha_i}$ for $i \neq 1$) are the minimum. The distance between atoms but the first atom ($d_{\mathbf{R}_i(J_i)\alpha_i, \mathbf{R}_j(J_j)\alpha_j}$ for $i, j \neq 1$) are not considered. This convention breaks the permutation symmetry in the infinite space because the first atom is treated differently. However, it satisfies ASR in the real space because the choice of $J_2, \cdots, J_n$ are uncorrelated so that

$$\sum_{\mathbf{R}_n J_n \alpha_n} \Phi_{\mu_1\cdots\mu_{n-1}\mu_n}(\mathbf{0}\alpha_1, \cdots, \mathbf{R}_{n-1}(J_{n-1})\alpha_{n-1}, \mathbf{R}_n(J_n)\alpha_n) \tag{D14}$$

is indepdent of $J_2, \cdots, J_{n-1}$.

In this research, we implement a program to the ALAMODE package to calculate IFCs which satisfy the permutation symmetry, ASR, and the space group symmetry in the infinite space. We first calculate $c_{\mathbf{R}_2\cdots\mathbf{R}_n,\alpha_1\cdots\alpha_n,\mu_1\cdots\mu_n}^{J_2\cdots J_n}$ to distribute equal values to the mirror images that the sum of the distance between all pairs is minimum. Then the IFCs in the supercell is calculated to satisfy the permutation symmetry and the space group symmetry in the supercell and the ASR in the real space (Eq. (D12)).

Appendix E: Test of the IFC renormalization by the strain

The IFC renormalization associated with the change of internal coordinates does not affect the fitting accuracy of the potential energy surface. This is because it does not alter the functional form of the potential energy surface. However, the IFC renormalization by the strain estimates the set of IFCs in deformed unit cells from the IFCs in the reference structure. Therefore, thorough tests are necessary to confirm the accuracy of the method.

We first cosider the harmonic IFCs of silicon. The harmonic phonon dispersions of silicon are calculated for lattice constants expanded by ± 2 % from the reference structure. As shown in Fig. 12, the phonon dispersions calculated by the IFC

renormalization (renormalized IFCs) correctly reproduce the results of DFT calculations at each lattice constant (IFCs extracted from DFT). In conjunction with the success of the IFC renormalization in calculating the thermal expansion (Fig. 2 in Section IV A), we can conclude that the IFC renormalization is accurate for weakly anharmonic materials, in which the low-order Taylor expansion accurately describes the potential energy surface.
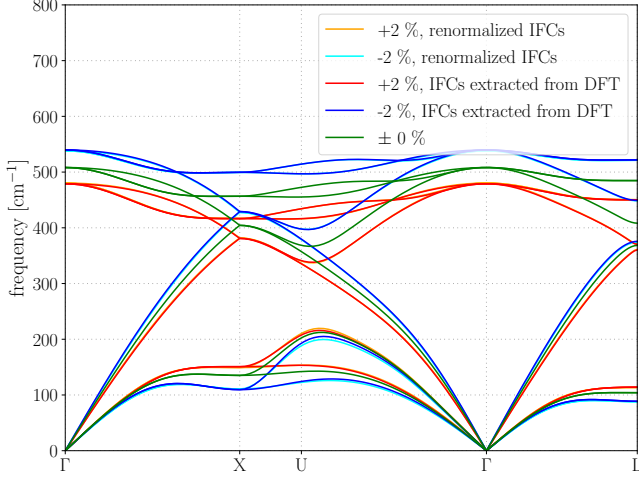

FIG. 12. The harmonic phonon dispersions of silicon in different lattice constants. $\pm 2\%$ means that lattice constant is expanded by $\pm 2\%$ from the reference structure. The calculation results of the IFC renormalization (renormalized IFCs) are compared with the results of DFT calculations at each lattice constant (IFCs extracted from DFT).

On the contrary, as shown in Fig. 13, the IFC renormalization by Eq. (13) overestimates the frequency shift of the soft mode of BaTiO$_3$. This can be because the up-to-quartic IFCs does not perfectly reproduce every detail of the complicated potential energy surface. Thus, the calculated IFCs cannot be extended for deformed cells, which is not included in the training data for the IFC calculation.

To avoid the error in the IFC renormalization, we directly calculate the strain-mode coupling $\left.\dfrac{\partial \widetilde{\Phi}_{\mu_1\mu_2}(\boldsymbol{R}_1\alpha_1, \boldsymbol{R}_2\alpha_2)}{\partial u_{\mu'_1\nu'_1}}\right|_{q^{(0)}=0, u_{\mu\nu}=0}$ by fitting the relation between the strain and the harmonic IFCs. These coupling constants are given as inputs independent from the IFCs. The harmonic IFCs are expected to change smoothly with cell deformation because the number of independent degrees of freedom is small and nonanalytic regularization terms are not used in the calculation. Replacing the strain-mode coupling in the RHS of Eq. (C13), we get Fig. 14, in which the change of harmonic dispersion is accurately reproduced with the IFC renormalization.

Besides, we check the accuracy of the renormalized anharmonic IFCs in BaTiO$_3$. Because it is difficult to directly visualize the anharmonic IFCs, we investigate the temperature dependence of the SCP frequency $\Omega_{\boldsymbol{k}\lambda}$, which reflects the significance of the quartic IFCs. The quartic IFCs are fixed
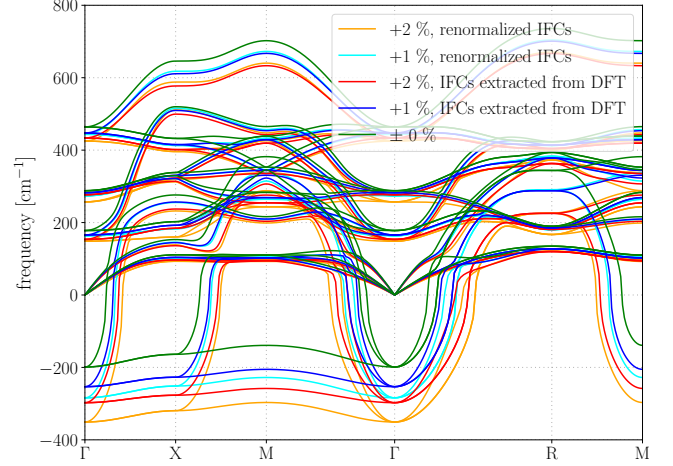

FIG. 13. Harmonic phonon dispersions of cubic BaTiO$_3$ in lattice constants expanded by 1% and 2% from the reference structure. The calculation results of the IFC renormalization (renormalized IFCs) are compared with the results of DFT calculations at each lattice constant (IFCs extracted from DFT).
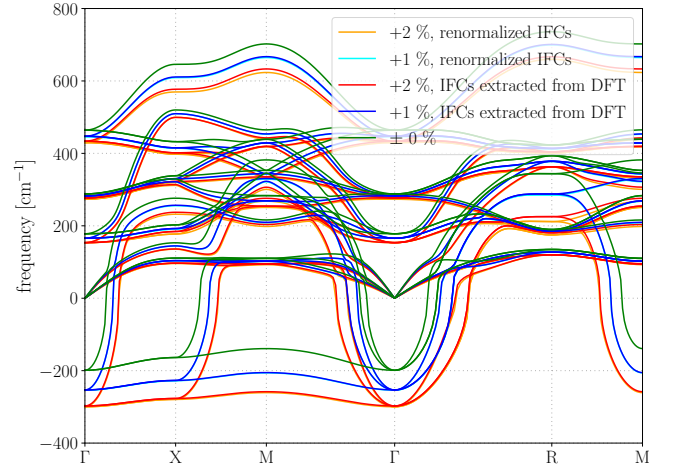

FIG. 14. Harmonic phonon dispersions of cubic BaTiO$_3$ in lattice constants expanded by 1% and 2% from the reference structure. The calculation results of the IFC renormalization (renormalized IFCs) are compared with the results of DFT calculations at each lattice constant (IFCs extracted from DFT). The strain-mode coupling constants are given as independent inputs in IFC renormalization.

in our calculation of IFC renormalization because the Taylor expansion is truncated at fourth order. As shown in Fig. 15, using fixed quartic IFCs has little effect on the SCP frequencies, which indicates that the IFC renormalization works accurately for the anharmonic IFCs of BaTiO$_3$.
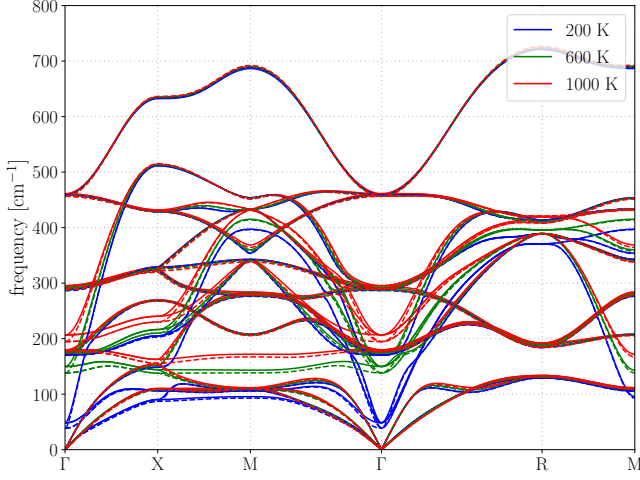
FIG. 15. Temperature dependence of the SCP frequency $\Omega_{\boldsymbol{k}\lambda}$ of cubic $BaTiO_3$ with the lattice constant expanded by 1 % from the reference structure. For the calculation of the solid lines, the harmonic IFCs for the expanded lattice constant and the quartic IFCs in the reference lattice constant are used. This corresponds to calculating quartic IFCs with IFC renormalization because the quartic IFCs are kept fixed in our calculation. For the calculation of dotted lines, the IFCs at the expanded lattice constant are used.

Appendix F: Test of convergence with respect to the cutoff radius and N_{max} in the IFC calculation

The cutoff radius and the maximum number of distinct atoms N_{max} involved in each IFC are adjustable parameters in the IFC calculation. The cutoff radius sets the maximum distance between the atoms. The IFCs are automatically set to zero for the combination of atoms that contains a pair whose distance is larger than the cutoff radius. Setting a larger cutoff enables more accurate fitting, but it also leads to higher computational costs.

Correspondingly, larger N_{max} means more degrees of freedom in fitting the displacement-force data. It makes the fitting more accurate but calculating the IFCs become more costly.

We change the cutoff radius and N_{max} of the quartic IFCs of $BaTiO_3$ to check the convergence of the calculation results, which results are shown in Figs. 16~18. The cutoff radius for the cubic IFCs is fixed to 15.0 Bohr, which is comparable to the size of the supercell. No cutoff radius is set for harmonic IFCs. $N_{\mathrm{max}} = 2, 3$ for harmonic and cubic IFCs, respectively, is employed, which does not impose any restrictions on these IFCs. Later in this Appendix, the cutoff and N_{max} refers to those for the quartic IFCs. We calculate the transitions between the cubic phase and each of the other three phases to take full advantage of crystal symmetry because the symmetry groups of rhombohedral and orthorhombic phases are not subgroups of that of orthorhombic and tetragonal phases respectively. The results in Figs. 16–18 are obtained by heating calculations, which is explained in Section IV B. In Figs. 16–18, the IFCs calculated by setting cutoff=9 Bohr, N_{max}=3 (solid line) and cutoff= 9 Bohr, N_{max}=4 (chain line) produces almost the same

result. This indicates that restricting the quartic IFCs to three-body ones ($N_{\mathrm{max}} = 3$) does not affect the calculation result, which is fortunate because setting $N_{\mathrm{max}} = 4$ with larger cutoff makes the calculation expensive. Comparing the results of different cutoff radii, we can see that the calculation results are convergent when cutoff= 12 Bohr. This also implies that the supercell is large enough because the calculation result converges with a cutoff which is smaller than the size of the supercell. Note that the length of a side of the $2 \times 2 \times 2$ supercell of $BaTiO_3$ is 7.9711 Å=15.063 Bohr. We use the IFCs calculated with cutoff= 15 Bohr, N_{max}=3 in the main part of this paper.
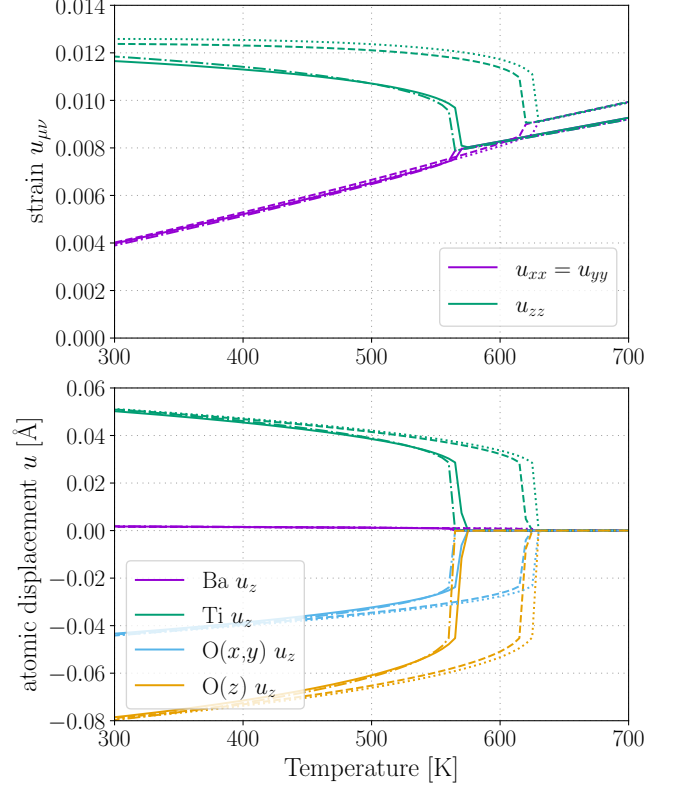

FIG. 16. Comparison of the T-dependent crystal structure of $BaTiO_3$ in its cubic-tetragonal phase transition with different settings in the IFC calculation. The pairs (cutoff radius, N_{max}) are (cutoff=9 Bohr, N_{max}=3) for the solid line, (cutoff= 12 Bohr, N_{max}=3) for the dashed line, (cutoff= 15 Bohr, N_{max}=3) for the dotted line, (cutoff= 9 Bohr, N_{max}=4) for the chain line. The nuclear quantum effect is taken into account in the calculations.

Appendix G: Test of convergence with respect to the number of k-points in the SCP calculation

In this Appendix, we check the convergence of the calculation results with respect to the number of k-points in the SCP calculation. We calculate the temperature-dependent crystal structure of $BaTiO_3$ in the transitions between the cubic phase and each of the other three phases, as in Appendix F. We
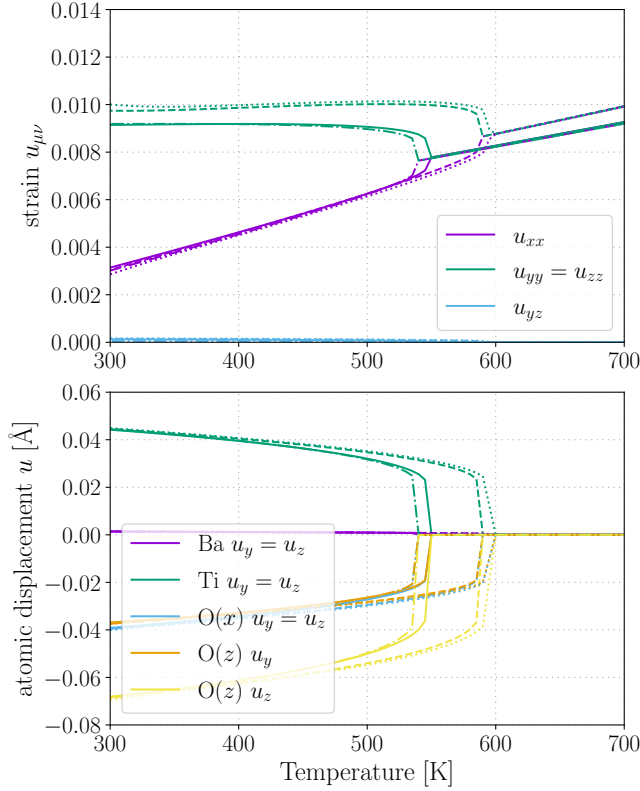
FIG. 17. The comparison of the T-dependent crystal structure of BaTiO$_3$ in the virtual cubic-orthorhombic phase transition with different settings in the IFC calculation. The pairs (cutoff radius, N_{max}) are (cutoff=9 Bohr, N_{max}=3) for the solid line, (cutoff= 12 Bohr, N_{max}=3) for the dashed line, (cutoff= 15 Bohr, N_{max}=3) for the dotted line, (cutoff= 9 Bohr, N_{max}=4) for the chain line. The nuclear quantum effect is taken into account in the calculations.

FIG. 18. The comparison of the T-dependent crystal structure of BaTiO$_3$ in the virtual cubic-rhombohedral phase transition with different settings in the IFC calculation. The pairs (cutoff radius, N_{max}) are (cutoff=9 Bohr, N_{max}=3) for the solid line, (cutoff= 12 Bohr, N_{max}=3) for the dashed line, (cutoff= 15 Bohr, N_{max}=3) for the dotted line, (cutoff= 9 Bohr, N_{max}=4) for the chain line. The nuclear quantum effect is taken into account in the calculations.

compare the result of heating calculations to check the convergence in low-symmetry phases in a wider temperature range. As depicted in Figs. 19–21, the calculation results is convergent with the $8 \times 8 \times 8$ k-mesh except in the very vicinity of the structural phase transition. We use $8 \times 8 \times 8$ k-mesh in the main text because the SCP calculation did not always show robust convergence when increasing the number of k-points. Improving the SCP solver to achieve more robust and efficient convergence is a topic of future research.

Appendix H: Test on the effect of the nonanalytic correction to the dynamical matrix

In the main text, we do not add the nonanalytic correction to the dynamical matrix in SCP calculations to enhance the convergence of the SCP calculations. Here, we check the effect of nonanalytic contribution by comparing the calculation results of the cubic-tetragonal transition, in which the calculation converged the most robustly. The nonanalytic contribution makes the calculation more unstable, presumably because the mixed-space approach [85] causes unreasonable curves in the
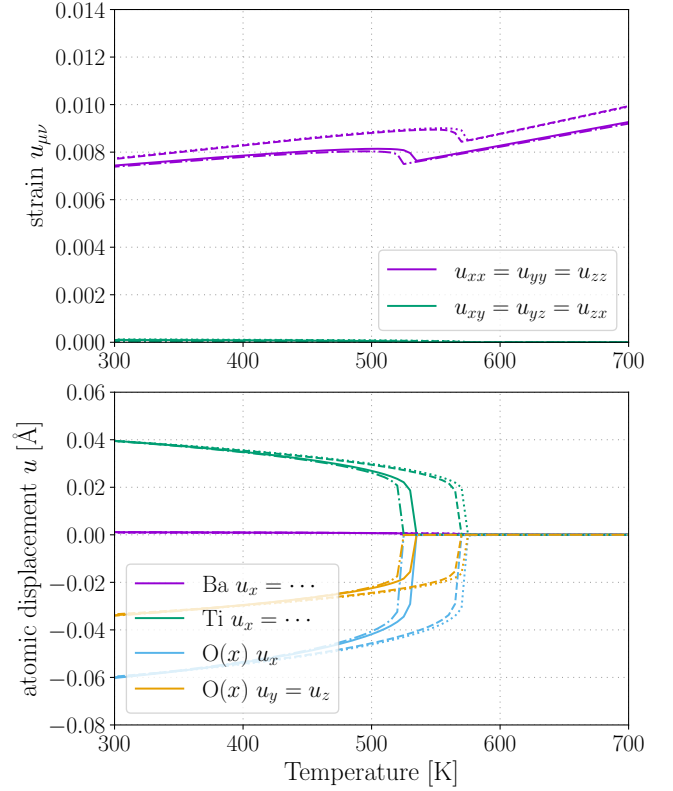
low-energy harmonic dispersions. As shown in Fig. 22, the nonanalytic contribution makes a small difference when the calculation converges, which validates the calculations without nonanalytic correction in the main text.

Appendix I: Test of convergence with respect to the size of the size of the supercell in IFC calculation

In order to check the convergence of the calculation results with respect to the size of the supercell in IFC calculation, we obtain the harmonic IFCs using the 4×4×4 supercell and use them in the structural optimization. We use the anharmonic IFCs calculated in the 2×2×2 supercell since the higher-order IFCs are more short-ranged in general. In addition, as discussed in Appendix F, the calculation results are fairly converged on the cutoff radius, which indirectly demonstrates the convergence on the supercell size for the anharmonic IFCs.

The comparison of the calculation results are shown in Figs. 23~25. Although the transition temperatures are shifted when changing the supercell size, the T-dependence of the crystal structure agrees well except in the vicinity of the struc-
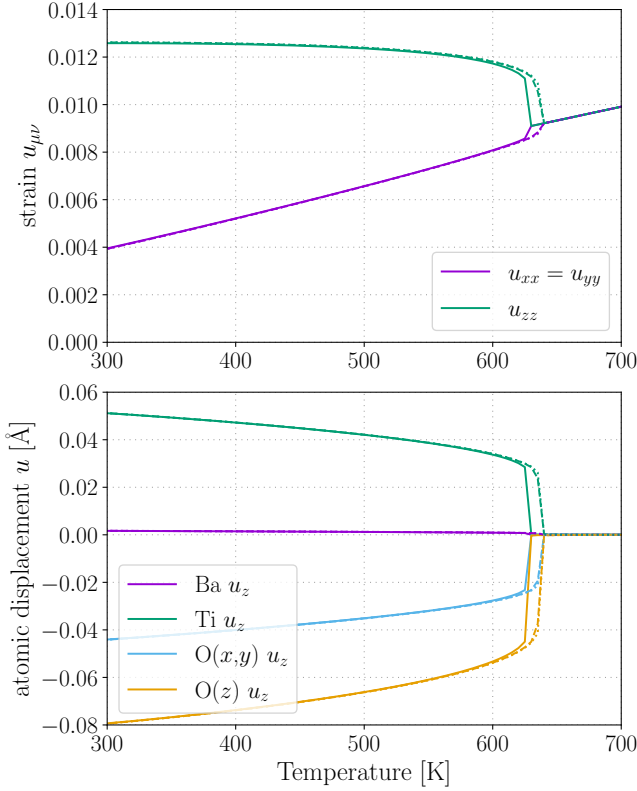
FIG. 19. The comparison of the T-dependent crystal structure of BaTiO$_3$ in the cubic-tetragonal phase transition with different number of k-points in the SCP calculation. The k-point mesh is $8 \times 8 \times 8$ for the solid line, $12 \times 12 \times 12$ for the dashed line, $16 \times 16 \times 16$ for the dotted line. The dotted line ($16 \times 16 \times 16$) almost completely overlaps with the dashed line ($12 \times 12 \times 12$). The nuclear quantum effect is taken into account in the calculations.

tural phase transitions. The differences in the transition temperatures are nearly 100 K, which is comparable to the error from the PBEsol functional. Note that the dependence on the DFT functionals will be much more prominent in general because the calculated transition temperatures are susceptible to the accuracy of the lattice constants.

Appendix J: Test on using the fixed Born effective charges in calculating the spontaneous polarization

In Section IV B 1, the spontaneous polarization is calculated with Eq. (25). Here, the Born effective charges $Z^*_{\alpha,\mu\nu}$ are fixed to the values at the reference cubic structure. In this appendix, we check the change of the Born effective charges at different phases and estimate the error of the spontaneous polarization.

We calculate the crystal structure in the three low-

temperature phases of BaTiO$_3$ by the structural optimization of DFT and calculate the Born effective charges at each phase. The optimum crystal structure in the tetragonal, orthorhombic, and rhombohedral phases are shown in Table III. Compared to the crystal structures at finite temperatures, we can see that the
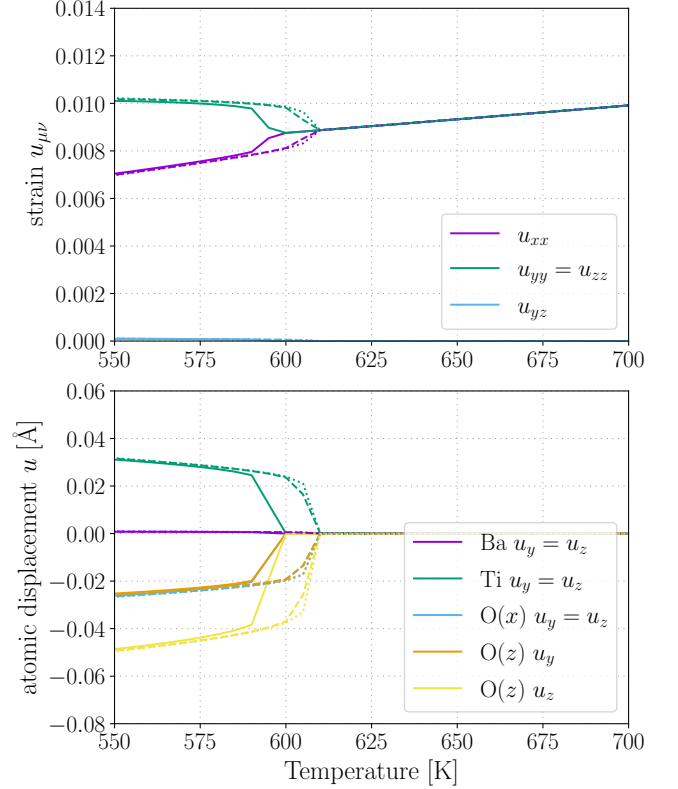

FIG. 20. The comparison of the T-dependent crystal structure of BaTiO$_3$ in the virtual cubic-orthorhombic phase transition with different number of k-points in the SCP calculation. The k-point mesh is $8 \times 8 \times 8$ for the solid line, $12 \times 12 \times 12$ for the dashed line, $16 \times 16 \times 16$ for the dotted line. The dotted line ($16 \times 16 \times 16$) almost completely overlaps with the dashed line ($12 \times 12 \times 12$). The nuclear quantum effect is taken into account in the calculations.

deviations from the cubic structure are about twice as large. The Born effective charges in the low-temperature phases are also shown in Tables III. Compared to those in the reference cubic structure, the Born effective charges in the direction of polarization gets smaller by about 20 % in the low-temperature phases. Thus, we estimate that the Born effective charges at the finite-temperature crystal structures are deviated by around $20/2 = 10$ % from those in the reference cubic structure. Since the spontaneous polarization is the integral of Born effective charges with respect to the structural changes, the error of the spontaneous polarization by using the fixed Born effective charge is around 5 %, which does not significantly affect the calculation results.

[1] W. J. Merz, The electric and optical behavior of BaTiO$_3$ single-domain crystals, Phys. Rev. **76**, 1221 (1949).

[2] H. Kay and P. Vousden, Xcv. symmetry changes in barium ti-

TABLE III. Summary of the lattice vectors and atomic displacements of cubic, tetragonal, orthorhombic, and rhombohedral BaTiO$_3$ obtained by the structural optimization at zero-temperature based on DFT. The Born effective charges computed using the optimized structures are also shown in units of the elementary charge e. The fractional coordinates of each atom in the cubic phase are as follows: Ba:$(0, 0, 0)$, Ti:$(\frac{1}{2}, \frac{1}{2}, \frac{1}{2})$, O(1):$(0, \frac{1}{2}, \frac{1}{2})$, O(2):$(\frac{1}{2}, 0, \frac{1}{2})$, O(3):$(\frac{1}{2}, \frac{1}{2}, 0)$.

	Cubic	Tetragonal	Orthorhombic	Rhombohedral
Lattice vectors [Å]				
a_1	(3.9855, 0.0000, 0.0000)	(3.9709, 0.0000, 0.0000)	(4.0170, 0.0062, 0.0000)	(4.0009, 0.0041, 0.0041)
a_2	(0.0000, 3.9855, 0.0000)	(0.0000, 3.9709, 0.0000)	(0.0062, 4.0170, 0.0000)	(0.0041, 4.0009, 0.0041)
a_3	(0.0000, 0.0000, 3.9855)	(0.0000, 0.0000, 4.0472)	(0.0000, 0.0000, 3.9658)	(0.0041, 0.0041, 4.0009)
Atomic displacements [Å]				
u_{Ba}	(0, 0, 0)	(0, 0, 0.0382)	(0.0297, 0.0297, 0)	(0.0249, 0.0249, 0.0249)
u_{Ti}	(0, 0, 0)	(0, 0, 0.0993)	(0.0809, 0.0809, 0)	(0.0690, 0.0690, 0.0690)
$u_{\text{O(1)}}$	(0, 0, 0)	(0, 0, −0.0235)	(−0.0533, −0.0146, 0)	(−0.0435, −0.0151, −0.0151)
$u_{\text{O(2)}}$	(0, 0, 0)	(0, 0, −0.0235)	(−0.0146, −0.0533, 0)	(−0.0151, −0.0435, −0.0151)
$u_{\text{O(3)}}$	(0, 0, 0)	(0, 0, −0.0702)	(−0.0225, −0.0225, 0)	(−0.0151, −0.0151, −0.0435)
Born effective charges [e]				
Z^*_{Ba}	(2.725, 0, 0) (0, 2.725, 0) (0, 0, 2.725)	(2.726, 0, 0) (0, 2.726, 0) (0, 0, 2.804)	(2.776, −0.016, 0) (−0.016, 2.776, 0) (0, 0, 2.728)	(2.763, −0.011, −0.011) (−0.011, 2.763, −0.011) (−0.011, −0.011, 2.763)
Z^*_{Ti}	(7.068, 0, 0) (0, 7.068, 0) (0, 0, 7.068)	(7.021, 0, 0) (0, 7.021, 0) (0, 0, 5.823)	(6.180, −0.319, 0) (−0.319, 6.180, 0) (0, 0, 7.018)	(6.400, −0.244, −0.244) (−0.244, 6.400, −0.244) (−0.244, −0.244, 6.400)
$Z^*_{\text{O(1)}}$	(−5.576, 0, 0) (0, −2.109, 0) (0, 0, −2.109)	(−5.606, 0, 0) (0, −2.098, 0) (0, 0, −1.983)	(−4.954, 0.088, 0) (0.266, −1.991, 0) (0, 0, −2.058)	(−5.135, 0.072, 0.072) (0.199, −2.014, −0.016) (0.199, −0.016, −2.014)
$Z^*_{\text{O(2)}}$	(−2.109, 0, 0) (0, −5.576, 0) (0, 0, −2.109)	(−2.098, 0, 0) (0, −5.606, 0) (0, 0, −1.983)	(−1.991, 0.266, 0) (0.088, −4.954, 0) (0, 0, −2.058)	(−2.014, 0.199, −0.016) (0.072, −5.135, 0.072) (−0.016, 0.199, −2.014)
$Z^*_{\text{O(3)}}$	(−2.109, 0, 0) (0, −2.109, 0) (0, 0, −5.576)	(−2.043, 0, 0) (0, −2.043, 0) (0, 0, −4.661)	(−2.010, −0.020, 0) (−0.020, −2.010, 0) (0, 0, −5.629)	(−2.014, −0.016, 0.199) (−0.016, −2.014, 0.199) (0.072, 0.072, −5.135)

tanate at low temperatures and their relation to its ferroelectric properties, The London, Edinburgh, and Dublin Philosophical Magazine and Journal of Science **40**, 1019 (1949), https://doi.org/10.1080/14786444908561371.

[3] R. E. Cohen, Origin of ferroelectricity in perovskite oxides, Nature **358**, 136 (1992).

[4] K. M. Rabe and P. Ghosez, First-principles studies of ferroelectric oxides, in Physics of Ferroelectrics: A Modern Perspective (Springer Berlin Heidelberg, Berlin, Heidelberg, 2007) pp. 117–174.

[5] Z. Xu, H. Yang, X. Song, Y. Chen, H. Yang, M. Liu, Z. Huang, Q. Zhang, J. Sun, L. Liu, and Y. Wang, Topical review: recent progress of charge density waves in 2D transition metal dichalcogenide-based heterojunctions and their applications, Nanotechnology **32**, 492001 (2021).

[6] M. D. Johannes and I. I. Mazin, Fermi surface nesting and the origin of charge density waves in metals, Phys. Rev. B **77**, 165135 (2008).

[7] M. Leroux, M. Le Tacon, M. Calandra, L. Cario, M.-A. Méasson, P. Diener, E. Borrissenko, A. Bosak, and P. Rodière, Anharmonic suppression of charge density waves in 2H-NbS$_2$, Phys. Rev. B **86**, 155125 (2012).

[8] R. Bianco, L. Monacelli, M. Calandra, F. Mauri, and I. Errea, Weak dimensionality dependence and dominant role of ionic fluctuations in the charge-density-wave transition of NbSe$_2$, Phys. Rev. Lett. **125**, 106101 (2020).

[9] J. A. Shaw and S. Kyriakides, Thermomechanical aspects of NiTi, Journal of the Mechanics and Physics of Solids **43**, 1243 (1995).

[10] J. B. Haskins, A. E. Thompson, and J. W. Lawson, Ab initio simulations of phase stability and martensitic transitions in NiTi, Phys. Rev. B **94**, 214110 (2016).

[11] W.-S. Ko, Temperature dependence of NiTi martensite structures: Density functional theory calculations, Scripta Materialia **154**, 134 (2018).

[12] M. H. Park, Y. H. Lee, T. Mikolajick, U. Schroeder, and C. S. Hwang, Review and perspective on ferroelectric hfo2-based thin films for memory applications, MRS Communications **8**, 795–808 (2018).

[13] M. Acosta, N. Novak, V. Rojas, S. Patel, R. Vaish, J. Koruza, G. A. Rossetti, and J. Rödel, BaTiO$_3$-based piezoelectrics: Fundamentals, current status, and perspectives, Applied Physics Reviews **4**, 041305 (2017), https://doi.org/10.1063/1.4990046.

[14] H. Li, R. Wang, S.-T. Han, and Y. Zhou, Ferroelectric polymers for non-volatile memory devices: a review, Polymer International **69**, 533 (2020), https://onlinelibrary.wiley.com/doi/pdf/10.1002/pi.5980.

[15] H. Liu, X. Yuan, P. Lu, X. Shi, F. Xu, Y. He, Y. Tang,
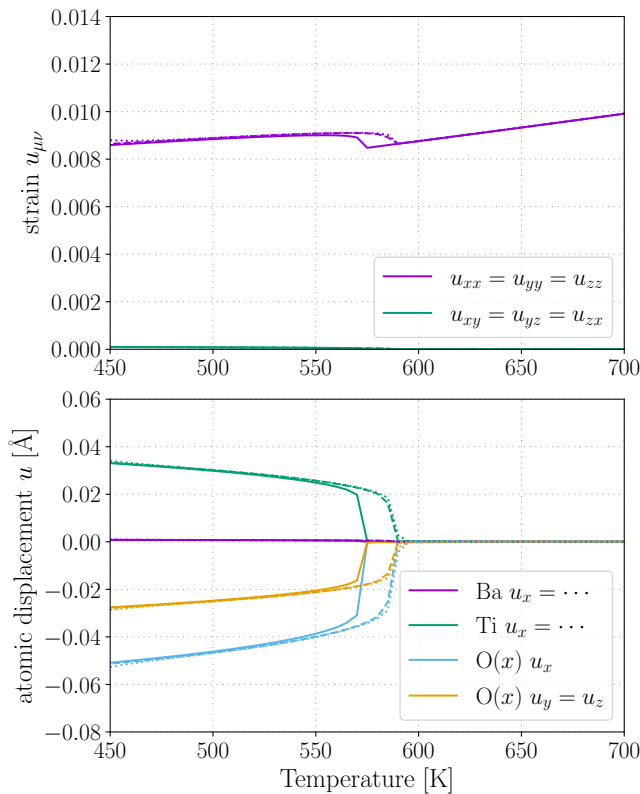
FIG. 21. The comparison of the T-dependent crystal structure of BaTiO$_3$ in the virtual cubic-rhombohedral phase transition with different number of k-points in the SCP calculation. The k-point mesh is $8 \times 8 \times 8$ for the solid line, $12 \times 12 \times 12$ for the dashed line, $16 \times 16 \times 16$ for the dotted line. The dotted line ($16 \times 16 \times 16$) almost completely overlaps with the dashed line ($12 \times 12 \times 12$). The nuclear quantum effect is taken into account in the calculations.
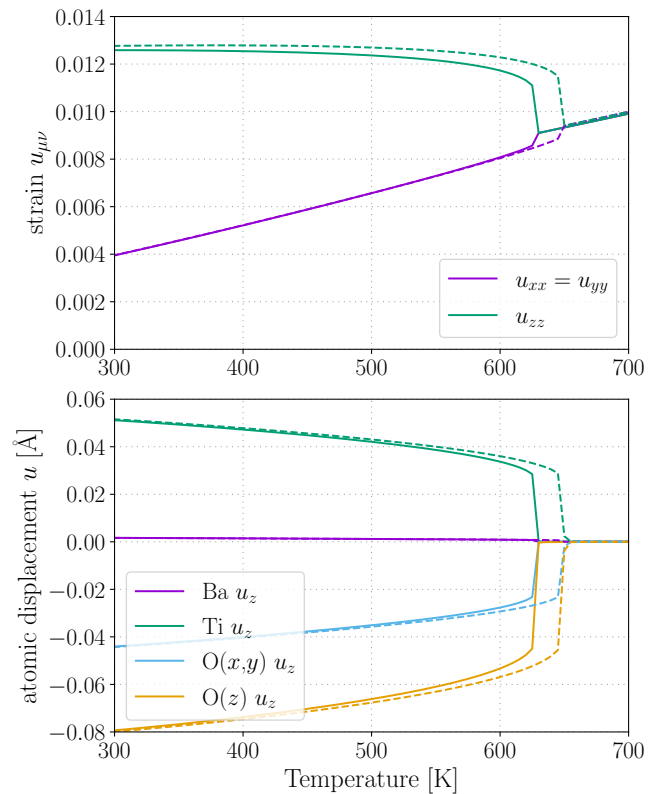
FIG. 22. The comparison of the T-dependent crystal structure of BaTiO$_3$ in the cubic-tetragonal phase transition with (the solid line) and without (the dashed line) nonanalytic correction to the dynamical matrix in SCP calculations. The nonanalytic correction is considered in the mixed-space approach [85]. The nuclear quantum effect is taken into account in the calculations.

S. Bai, W. Zhang, L. Chen, Y. Lin, L. Shi, H. Lin, X. Gao, X. Zhang, H. Chi, and C. Uher, Ultrahigh thermoelectric performance by electron and phonon critical scattering in Cu$_2$Se$_{1-x}$I$_x$, Advanced Materials **25**, 6607 (2013), https://onlinelibrary.wiley.com/doi/pdf/10.1002/adma.201302660.

[16] H. Sakai, K. Ikeura, M. S. Bahramy, N. Ogawa, D. Hashizume, J. Fujioka, Y. Tokura, and S. Ishiwata, Critical enhancement of thermopower in a chemically tuned polar semimetal MoTe$_2$, Science Advances **2**, e1601378 (2016), https://www.science.org/doi/pdf/10.1126/sciadv.1601378.

[17] H. Takahashi, K. Hasegawa, T. Akiba, H. Sakai, M. S. Bahramy, and S. Ishiwata, Giant enhancement of cryogenic thermopower by polar structural instability in the pressurized semimetal MoTe$_2$, Phys. Rev. B **100**, 195130 (2019).

[18] C. Setty, M. Baggioli, and A. Zaccone, Superconducting dome in ferroelectric-type materials from soft mode instability, Phys. Rev. B **105**, L020506 (2022).

[19] C. Setty, M. Baggioli, and A. Zaccone, Anharmonic theory of superconductivity in the high-pressure materials, Phys. Rev. B **103**, 094519 (2021).

[20] A. P. Drozdov, M. I. Eremets, I. A. Troyan, V. Ksenofontov, and S. I. Shylin, Conventional superconductivity at 203 kelvin at high pressures in the sulfur hydride system, Nature **525**, 73 (2015).

[21] A. P. Drozdov, P. P. Kong, V. S. Minkov, S. P. Besedin, M. A. Kuzovnikov, S. Mozaffari, L. Balicas, F. F. Balakirev, D. E. Graf, V. B. Prakapenka, E. Greenberg, D. A. Knyazev, M. Tkacz, and M. I. Eremets, Superconductivity at 250 K in lanthanum hydride under high pressures, Nature **569**, 528 (2019).

[22] M. Somayazulu, M. Ahart, A. K. Mishra, Z. M. Geballe, M. Baldini, Y. Meng, V. V. Struzhkin, and R. J. Hemley, Evidence for superconductivity above 260 K in lanthanum superhydride at megabar pressures, Phys. Rev. Lett. **122**, 027001 (2019).

[23] L. Ma, K. Wang, Y. Xie, X. Yang, Y. Wang, M. Zhou, H. Liu, X. Yu, Y. Zhao, H. Wang, G. Liu, and Y. Ma, High-temperature superconducting phase in clathrate calcium hydride CaH$_6$ up to 215 K at a pressure of 172 GPa, Phys. Rev. Lett. **128**, 167001 (2022).

[24] J. A. Flores-Livas, L. Boeri, A. Sanna, G. Profeta, R. Arita, and M. Eremets, A perspective on conventional high-temperature superconductors at high pressure: Methods and materials, Physics Reports **856**, 1 (2020).

[25] A. K. Jena, A. Kulkarni, and T. Miyasaka, Halide perovskite photovoltaics: Background, status, and future prospects, Chemical Reviews **119**, 3036 (2019), https://doi.org/10.1021/acs.chemrev.8b00539.

[26] T. Lanigan-Atkins, X. He, M. J. Krogstad, D. M. Pajerowski, D. L. Abernathy, G. N. M. N. Xu, Z. Xu, D.-Y. Chung, M. G. Kanatzidis, S. Rosenkranz, R. Osborn, and O. Delaire, Two-
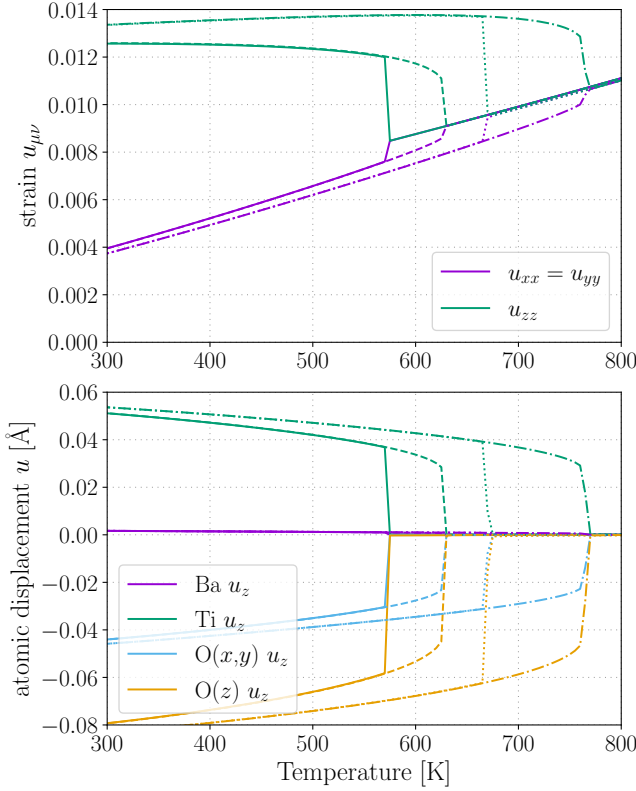
FIG. 23. The comparison of the T-dependent crystal structure of BaTiO$_3$ in the cubic-tetragonal phase transition using IFCs calculated in different supercells. The solid line and the dashed lines represent the cooling and heating calculation with harmonic IFCs calculated in the 2×2×2 supercell, respectively. The dotted line and the chain line are the cooling and heating calculations with harmonic IFCs calculated in the 4×4×4 supercell. The nuclear quantum effect is taken into account in the calculations.
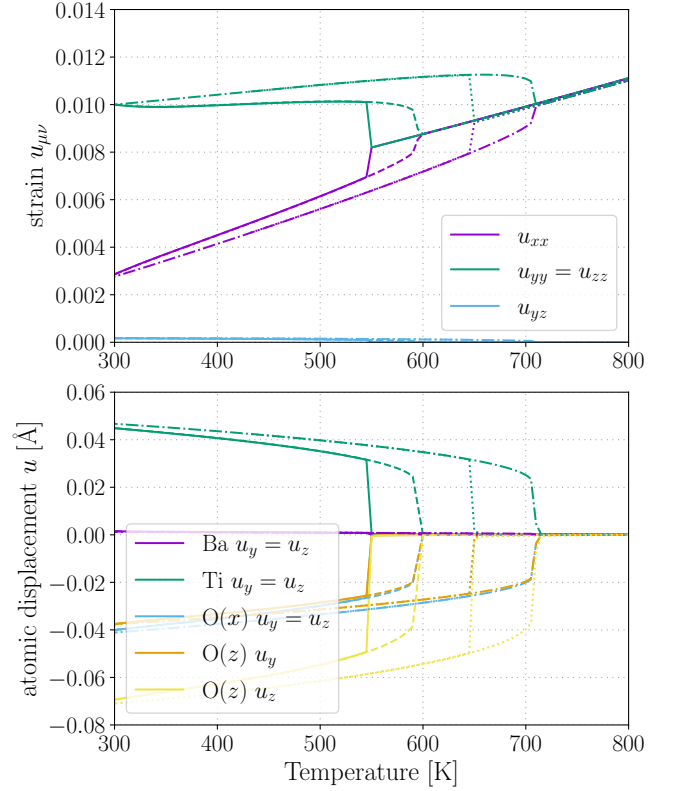
FIG. 24. The comparison of the T-dependent crystal structure of BaTiO$_3$ in the virtual cubic-orthorhombic phase transition using IFCs calculated in different supercells. The solid line and the dashed lines represent the cooling and heating calculation with harmonic IFCs calculated in the 2×2×2 supercell, respectively. The dotted line and the chain line are the cooling and heating calculations with harmonic IFCs calculated in the 4×4×4 supercell. The nuclear quantum effect is taken into account in the calculations.

dimensional overdamped fluctuations of the soft perovskite lattice in CsPbBr$_3$, Nature Materials **20**, 977 (2021).

[27] G. Kresse and J. Furthmüller, Efficient iterative schemes for ab initio total-energy calculations using a plane-wave basis set, Phys. Rev. B **54**, 11169 (1996).

[28] P. Giannozzi, S. Baroni, N. Bonini, M. Calandra, R. Car, C. Cavazzoni, D. Ceresoli, G. L. Chiarotti, M. Cococcioni, I. Dabo, A. D. Corso, S. de Gironcoli, S. Fabris, G. Fratesi, R. Gebauer, U. Gerstmann, C. Gougoussis, A. Kokalj, M. Lazzeri, L. Martin-Samos, N. Marzari, F. Mauri, R. Mazzarello, S. Paolini, A. Pasquarello, L. Paulatto, C. Sbraccia, S. Scandolo, G. Sclauzero, A. P. Seitsonen, A. Smogunov, P. Umari, and R. M. Wentzcovitch, QUANTUM ESPRESSO: a modular and open-source software project for quantum simulations of materials, Journal of Physics: Condensed Matter **21**, 395502 (2009).

[29] P. Giannozzi, O. Andreussi, T. Brumme, O. Bunau, M. B. Nardelli, M. Calandra, R. Car, C. Cavazzoni, D. Ceresoli, M. Cococcioni, N. Colonna, I. Carnimeo, A. D. Corso, S. de Gironcoli, P. Delugas, R. A. DiStasio, A. Ferretti, A. Floris, G. Fratesi, G. Fugallo, R. Gebauer, U. Gerstmann, F. Giustino, T. Gorni, J. Jia, M. Kawamura, H.-Y. Ko, A. Kokalj, E. Küçükbenli, M. Lazzeri, M. Marsili, N. Marzari, F. Mauri, N. L. Nguyen, H.-

V. Nguyen, A. O. de-la Roza, L. Paulatto, S. Poncé, D. Rocca, R. Sabatini, B. Santra, M. Schlipf, A. P. Seitsonen, A. Smogunov, I. Timrov, T. Thonhauser, P. Umari, N. Vast, X. Wu, and S. Baroni, Advanced capabilities for materials modelling with quantum ESPRESSO, Journal of Physics: Condensed Matter **29**, 465901 (2017).

[30] S. Poncé, E. Margine, C. Verdi, and F. Giustino, EPW: Electron–phonon coupling, transport and superconducting properties using maximally localized Wannier functions, Computer Physics Communications **209**, 116 (2016).

[31] J. Noffsinger, F. Giustino, B. D. Malone, C.-H. Park, S. G. Louie, and M. L. Cohen, EPW: A program for calculating the electron–phonon coupling using maximally localized Wannier functions, Computer Physics Communications **181**, 2140 (2010).

[32] G. Pizzi, V. Vitale, R. Arita, S. Blügel, F. Freimuth, G. Géranton, M. Gibertini, D. Gresch, C. Johnson, T. Koretsune, J. Ibañez-Azpiroz, H. Lee, J.-M. Lihm, D. Marchand, A. Marrazzo, Y. Mokrousov, J. I. Mustafa, Y. Nohara, Y. Nomura, L. Paulatto, S. Poncé, T. Ponweiser, J. Qiao, F. Thöle, S. S. Tsirkin, M. Wierzbowska, N. Marzari, D. Vanderbilt, I. Souza, A. A. Mostofi, and J. R. Yates, Wannier90 as a community code: new features and applications, Journal of Physics: Condensed Matter
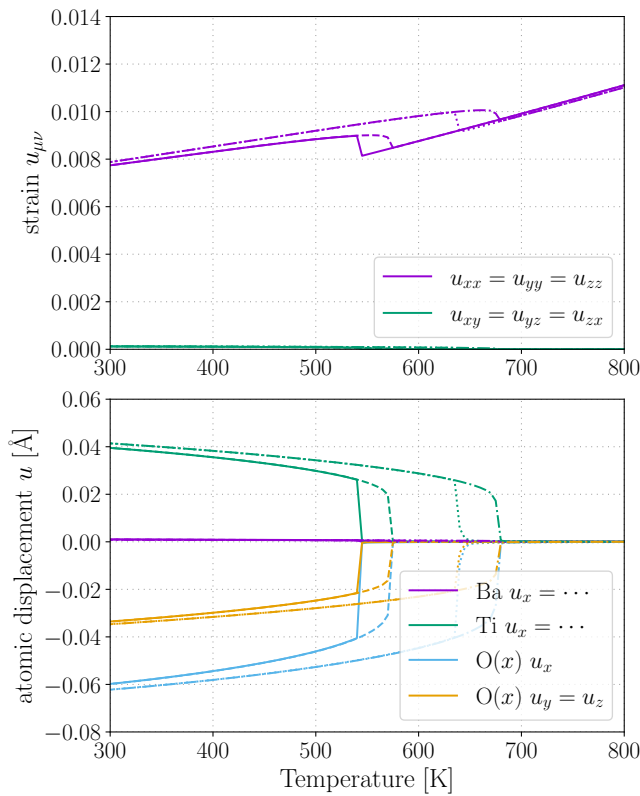
FIG. 25. The comparison of the T-dependent crystal structure of BaTiO$_3$ in the virtual cubic-rhombohedral phase transition using IFCs calculated in different supercells. The solid line and the dashed lines represent the cooling and heating calculation with harmonic IFCs calculated in the 2×2×2 supercell, respectively. The dotted line and the chain line are the cooling and heating calculations with harmonic IFCs calculated in the 4×4×4 supercell. The nuclear quantum effect is taken into account in the calculations.

32, 165902 (2020).

[33] A. A. Mostofi, J. R. Yates, G. Pizzi, Y.-S. Lee, I. Souza, D. Vanderbilt, and N. Marzari, An updated version of wannier90: A tool for obtaining maximally-localised Wannier functions, Computer Physics Communications **185**, 2309 (2014).

[34] O. Hellman, I. A. Abrikosov, and S. I. Simak, Lattice dynamics of anharmonic solids from first principles, Phys. Rev. B **84**, 180301 (2011).

[35] P. Souvatzis, O. Eriksson, M. I. Katsnelson, and S. P. Rudin, Entropy driven stabilization of energetically unstable crystal structures explained from first principles theory, Phys. Rev. Lett. **100**, 095901 (2008).

[36] G. A. S. Ribeiro, L. Paulatto, R. Bianco, I. Errea, F. Mauri, and M. Calandra, Strong anharmonicity in the phonon spectra of PbTe and SnTe from first principles, Phys. Rev. B **97**, 014306 (2018).

[37] T. Tadano and S. Tsuneyuki, Self-consistent phonon calculations of lattice dynamical properties in cubic SrTiO$_3$ with first-principles anharmonic force constants, Phys. Rev. B **92**, 054301 (2015).

[38] M. Rossi, P. Gasparotto, and M. Ceriotti, Anharmonic and quantum fluctuations in molecular crystals: A first-principles study of the stability of paracetamol, Phys. Rev. Lett. **117**, 115702 (2016).

[39] A. Perez, M. E. Tuckerman, H. P. Hjalmarson, and O. A. von Lilienfeld, Enol tautomers of Watson-Crick base pair models are metastable because of nuclear quantum effects, Journal of the American Chemical Society **132**, 11510 (2010), pMID: 20681591, https://doi.org/10.1021/ja102004b.

[40] I. Errea, F. Belli, L. Monacelli, A. Sanna, T. Koretsune, T. Tadano, R. Bianco, M. Calandra, R. Arita, F. Mauri, and J. A. Flores-Livas, Quantum crystal structure in the 250-kelvin superconducting lanthanum hydride, Nature **578**, 66 (2020).

[41] J. Íñiguez and D. Vanderbilt, First-principles study of the temperature-pressure phase diagram of BaTiO$_3$, Phys. Rev. Lett. **89**, 115503 (2002).

[42] J. Behler and M. Parrinello, Generalized neural-network representation of high-dimensional potential-energy surfaces, Phys. Rev. Lett. **98**, 146401 (2007).

[43] J. Behler, Constructing high-dimensional neural network potentials: A tutorial review, International Journal of Quantum Chemistry **115**, 1032 (2015), https://onlinelibrary.wiley.com/doi/pdf/10.1002/qua.24890.

[44] R. Jinnouchi, F. Karsai, and G. Kresse, On-the-fly machine learning force field generation: Application to melting points, Phys. Rev. B **100**, 014105 (2019).

[45] L. Gigli, M. Veit, M. Kotiuga, G. Pizzi, N. Marzari, and M. Ceriotti, Thermodynamics and dielectric response of BaTiO$_3$ by data-driven modeling, npj Computational Materials **8**, 209 (2022).

[46] D. J. Hooton, The use of a model in anharmonic lattice dynamics, The Philosophical Magazine: A Journal of Theoretical Experimental and Applied Physics **3**, 49 (1958), https://doi.org/10.1080/14786435808243224.

[47] N. R. Werthamer, Self-consistent phonon formulation of anharmonic lattice dynamics, Phys. Rev. B **1**, 572 (1970).

[48] T. R. Koehler, Theory of the self-consistent harmonic approximation with application to solid neon, Phys. Rev. Lett. **17**, 89 (1966).

[49] N. S. Gillis, N. R. Werthamer, and T. R. Koehler, Properties of crystalline argon and neon in the self-consistent phonon approximation, Phys. Rev. **165**, 951 (1968).

[50] T. Tadano and S. Tsuneyuki, Quartic anharmonicity of rattlers and its effect on lattice thermal conductivity of clathrates from first principles, Phys. Rev. Lett. **120**, 105901 (2018).

[51] U. Aseginolaza, R. Bianco, L. Monacelli, L. Paulatto, M. Calandra, F. Mauri, A. Bergara, and I. Errea, Phonon collapse and second-order phase transition in thermoelectric SnSe, Phys. Rev. Lett. **122**, 075901 (2019).

[52] P. Souvatzis, O. Eriksson, M. Katsnelson, and S. Rudin, The self-consistent ab initio lattice dynamical method, Computational Materials Science **44**, 888 (2009).

[53] A. van Roekeghem, J. Carrete, and N. Mingo, Quantum self-consistent ab-initio lattice dynamics, Computer Physics Communications **263**, 107945 (2021).

[54] L. Monacelli, R. Bianco, M. Cherubini, M. Calandra, I. Errea, and F. Mauri, The stochastic self-consistent harmonic approximation: calculating vibrational properties of materials with full quantum and anharmonic effects, Journal of Physics: Condensed Matter **33**, 363001 (2021).

[55] T. Tadano, Y. Gohda, and S. Tsuneyuki, Anharmonic force constants extracted from first-principles molecular dynamics: applications to heat transfer simulations, Journal of Physics: Condensed Matter **26**, 225402 (2014).

[56] T. Tadano and S. Tsuneyuki, First-principles lattice dynamics method for strongly anharmonic crystals, Journal of the Physical Society of Japan **87**, 041015 (2018),

https://doi.org/10.7566/JPSJ.87.041015.

[57] Y. Oba, T. Tadano, R. Akashi, and S. Tsuneyuki, First-principles study of phonon anharmonicity and negative thermal expansion in ScF$_3$, Phys. Rev. Materials **3**, 033601 (2019).

[58] F. Jona and G. Shirane, Ferroelectric Crystals, Dover books on engineering (Dover Publications, 1993).

[59] M. Lines and A. Glass, Principles and Applications of Ferroelectrics and Related Materials, International series of monographs on physics (OUP Oxford, 2001).

[60] D. C. Wallace, Thermodynamics of crystals, American Journal of Physics **40**, 1718 (1972).

[61] F. Zhou, W. Nielson, Y. Xia, and V. Ozoliņš, Lattice anharmonicity and thermal conductivity from compressive sensing of first-principles calculations, Phys. Rev. Lett. **113**, 185501 (2014).

[62] F. Zhou, W. Nielson, Y. Xia, and V. Ozoliņš, Compressive sensing lattice dynamics. I. general formalism, Phys. Rev. B **100**, 184308 (2019).

[63] J. Zhao, J. M. Winey, and Y. M. Gupta, First-principles calculations of second- and third-order elastic constants for single crystals of arbitrary symmetry, Phys. Rev. B **75**, 094105 (2007).

[64] M. Liao, Y. Liu, S.-L. Shang, F. Zhou, N. Qu, Y. Chen, Z. Lai, Z.-K. Liu, and J. Zhu, Elastic3rd: A tool for calculating third-order elastic constants from first-principles calculations, Computer Physics Communications **261**, 107777 (2021).

[65] J. P. Perdew, A. Ruzsinszky, G. I. Csonka, O. A. Vydrov, G. E. Scuseria, L. A. Constantin, X. Zhou, and K. Burke, Restoring the density-gradient expansion for exchange in solids and surfaces, Phys. Rev. Lett. **100**, 136406 (2008).

[66] P. E. Blöchl, Projector augmented-wave method, Phys. Rev. B **50**, 17953 (1994).

[67] G. Kresse and D. Joubert, From ultrasoft pseudopotentials to the projector augmented-wave method, Phys. Rev. B **59**, 1758 (1999).

[68] F. Birch, Finite elastic strain of cubic crystals, Phys. Rev. **71**, 809 (1947).

[69] F. D. Murnaghan, The compressibility of media under extreme pressures, Proceedings of the National Academy of Sciences **30**, 244 (1944), https://www.pnas.org/doi/pdf/10.1073/pnas.30.9.244.

[70] R. Masuki, T. Nomoto, R. Arita, and T. Tadano, Anharmonic Grüneisen theory based on self-consistent phonon theory: Impact of phonon-phonon interactions neglected in the quasiharmonic theory, Phys. Rev. B **105**, 064112 (2022).

[71] T. Middelmann, A. Walkov, G. Bartl, and R. Schödel, Thermal expansion coefficient of single-crystal silicon from 7 K to 293 K, Phys. Rev. B **92**, 174113 (2015).

[72] Y. Okada and Y. Tokumaru, Precise determination of lattice parameter and thermal expansion coefficient of silicon between 300 and 1500 K, Journal of Applied Physics **56**, 314 (1984), https://doi.org/10.1063/1.333965.

[73] W. Zhong, D. Vanderbilt, and K. M. Rabe, First-principles theory of ferroelectric phase transitions for perovskites: The case of BaTiO$_3$, Phys. Rev. B **52**, 6301 (1995).

[74] W. Zhong, D. Vanderbilt, and K. M. Rabe, Phase transitions in BaTiO$_3$ from first principles, Phys. Rev. Lett. **73**, 1861 (1994).

[75] S. Baroni and R. Resta, Ab initio calculation of the macroscopic dielectric constant in silicon, Phys. Rev. B **33**, 7017 (1986).

[76] M. Gajdoš, K. Hummer, G. Kresse, J. Furthmüller, and F. Bechstedt, Linear optical properties in the projector-augmented wave methodology, Phys. Rev. B **73**, 045112 (2006).

[77] G.-X. Zhang, A. M. Reilly, A. Tkatchenko, and M. Scheffler, Performance of various density-functional approximations for cohesive properties of 64 bulk solids, New Journal of Physics **20**, 063020 (2018).

[78] T. Ishidate, S. Abe, H. Takahashi, and N. Môri, Phase diagram of BaTiO$_3$, Phys. Rev. Lett. **78**, 2397 (1997).

[79] A. S. Chaves, F. C. S. Barreto, R. A. Nogueira, and B. Zẽks, Thermodynamics of an eight-site order-disorder model for ferroelectrics, Phys. Rev. B **13**, 207 (1976).

[80] M. Paściak, T. R. Welberry, J. Kulda, S. Leoni, and J. Hlinka, Dynamic displacement disorder of cubic BaTiO$_3$, Phys. Rev. Lett. **120**, 167601 (2018).

[81] Y. Qi, S. Liu, I. Grinberg, and A. M. Rappe, Atomistic description for temperature-driven phase transitions in BaTiO$_3$, Phys. Rev. B **94**, 134308 (2016).

[82] Y. Yamada, G. Shirane, and A. Linz, Study of critical fluctuations in BaTiO$_3$ by neutron scattering, Phys. Rev. **177**, 848 (1969).

[83] H. Vogt, J. A. Sanjurjo, and G. Rossbroich, Soft-mode spectroscopy in cubic BaTiO$_3$ by hyper-raman scattering, Phys. Rev. B **26**, 5904 (1982).

[84] I. Errea, M. Calandra, and F. Mauri, Anharmonic free energies and phonon dispersions from the stochastic self-consistent harmonic approximation: Application to platinum and palladium hydrides, Phys. Rev. B **89**, 064302 (2014).

[85] Y. Wang, J. J. Wang, W. Y. Wang, Z. G. Mei, S. L. Shang, L. Q. Chen, and Z. K. Liu, A mixed-space approach to first-principles calculations of phonon frequencies for polar materials, Journal of Physics: Condensed Matter **22**, 202201 (2010).